

Using VO tools to investigate distant radio starbursts hosting obscured AGN in the HDF(N) region

A. M. S. Richards¹, T. W. B. Muxlow¹, R. Beswick¹, M. G. Allen², K. Benson³, R. C. Dickson¹, M. A. Garrett⁴, S. T. Garrington¹, E. Gonzalez-Solarez⁵, P. A. Harrison⁶, A. J. Holloway¹, M. M. Kettenis⁴, R. A. Laing⁶, E. A. Richards⁷, H. Thrall¹, H. J. van Langevelde^{4,8}, N. A. Walton⁵, P. N. Wilkinson¹ and N. Winstanley¹.

¹ Jodrell Bank Observatory, University of Manchester, SK11 9DL, Macclesfield, UK.

² Centre de Données astronomiques de Strasbourg (UMR 7550), F-67000, Strasbourg, France.

³ Mullard Space Science Laboratory, UCL, Holmbury St. Mary, Dorking, Surrey, RH5 6NT, UK.

⁴ Joint Institute for VLBI in Europe, Postbus 2, 7990 AA Dwingeloo, The Netherlands.

⁵ Institute of Astronomy, Madingley Road, Cambridge, CB3 0HA, UK.

⁶ European Southern Observatory, D-85748 Garching bei München, Germany.

⁷ Department of Physics, Talledega College, Talledega, Alabama 35160, USA.

⁸ Sterrewacht Leiden, Leiden University, Postbus 9513, 2300 RA Leiden, The Netherlands.

Received August 1, 2005; accepted March 16, 2005

ABSTRACT

Context. A 10-arcmin region around the Hubble Deep Field (North) contains 92 radio sources brighter than 40 μ Jy which are well-resolved by MERLIN+VLA at 0'2-2'' resolution (average size $\sim 1''$). 55 of these have *Chandra* X-ray counterparts in the 2-Ms CDF(N) field including at least 17 with a hard X-ray photon index and high luminosity characteristic of a type-II (obscured) AGN. More than 70% of the radio sources have been classified as starbursts or AGN using radio morphologies, spectral indices and comparisons with optical appearance and rest-frame MIR emission. On this basis, starbursts outnumber radio AGN 3:1.

Aims. We investigate the possibility that very luminous radio and X-ray emission originates from different phenomena in the same high-redshift galaxies.

Methods. This study extends the Virtual Observatory (VO) methods previously used to identify X-ray-selected obscured type-II AGN, to examine the relationship between radio and X-ray emission. We describe a VO cut-out server for MERLIN+VLA 1.4-GHz radio images in the HDF(N) region.

Results. The high-redshift starbursts have typical sizes of 5–10 kpc and star formation rates of $\sim 1000 M_{\odot} \text{ yr}^{-1}$, an order of magnitude more extended and intense than in the local universe. There is no obvious correlation between radio and X-ray luminosities nor spectral indices at $z \gtrsim 1.3$. About 70% of both the radio-selected AGN and the starburst samples were detected by *Chandra*. The X-ray luminosity indicates the presence of an AGN in at least half of the 45 cross-matched radio starbursts. Eleven of these are type-II AGN, of which 7 are at $z \geq 1.5$. This distribution overlaps closely with the X-ray detected radio sources which were also detected by SCUBA. In contrast, all but one of the AGN-dominated radio sources are at $z < 1.5$, including the 4 which are also X-ray selected type-II AGN. The stacked 1.4-GHz emission at the positions of radio-faint X-ray sources is correlated with X-ray hardness.

Conclusions. Almost all extended radio starbursts at $z > 1.3$ host X-ray selected obscured AGN. The radio emission from most of these ultra-luminous objects is dominated by star formation although the highest redshift ($z = 4.424$) source has a substantial AGN contribution. Star-formation appears to contribute less than 1/3 of their X-ray luminosity. Our results support the inferences from SCUBA and IR data, that at $z \gtrsim 1.5$, star formation is observably more extended and more copious, it is closely linked to AGN activity and it is triggered differently, compared with star formation at lower redshifts.

Key words. Astronomical data bases: miscellaneous – X-rays: galaxies – radio continuum: galaxies – galaxies: active – galaxies: starburst – galaxies: evolution

1. Introduction

There is now general agreement that the number of vigorous star-forming galaxies, and the star formation rate (SFR) within these galaxies, increases dramatically at $z > 1$. The details of how these starburst galaxies relate to the high redshift Active Galactic Nucleus (AGN) population are less clear. Objects detected individually at $z > 1$ in radio and X-rays, by even the deepest available exposures, are inevitably abnormally luminous. Is it equally inevitable that, in a galaxy detected in both regimes, all such bright emission emanates from the same phenomenon, or

can we separate contributions from AGN and from starbursts if these coexist?

The unprecedentedly sensitive observations of the Hubble Deep Field (North) (HDF(N))¹ which commenced in 1996 provided the first detailed attempts to quantify the star formation history of the universe (Madau et al. 1996). The radio luminosity function evolves rapidly with redshift, as $(1+z)^3$ for $0.5 < z < 1.5$ (Cowie et al. 2004a). Subsamples classified using optical spectra and X-ray power suggest that the AGN luminos-

¹ We use the term HDF(N) to describe observations made in and around the original HDF; these form part of the multi-wavelength GOODS (Great Observatories Origins Deep Surveys) project (Giavalisco et al. 2004).

ity function is declining at $z > 0.9$ compared to lower redshifts, while the reverse is the case for star-forming galaxies. This is supported by *Spitzer* detections of Ultra-Luminous IR Galaxies (ULIRGs) with IR luminosities $> 10^{12} M_{\odot}$. These show that the co-moving density of ULIRGs (with a typical SFR of $200\text{--}300 M_{\odot} \text{ yr}^{-1}$) at $z \sim 2$ was at least 3 orders of magnitude greater than in the local universe (Daddi et al. 2005).

Star-formation rates (SFR) measured from optical data only can be greatly underestimated or overlooked altogether (Reddy & Steidel 2004). For example, Cowie et al. (2004a), using optical spectra, were only able to classify 53% of the radio sources $< 100 \mu\text{Jy}$ in the HDF(N), finding that 28% are star-forming galaxies. In contrast, over 2/3 of the 58 resolved sources $< 100 \mu\text{Jy}$ in the HDF(N) were classified using the radio-based criteria of Muxlow et al. (2005), containing 60% starbursts. Similarly, up to 90% of the distant or obscured AGN revealed by deep X-ray observations may be missed by optical surveys (Bauer et al. 2004).

Classification based on IR, sub-mm and radio properties is favoured because local starburst galaxies show a strong peak in their spectral energy distributions (SED) around 3 THz ($100 \mu\text{m}$) (e.g. Yun & Carilli 2002) which can be used to estimate the SFR (Condon 1992; Cram et al. 1998; Yun et al. 2001). The most striking evidence for extraordinary levels of high-redshift star formation came from Sub-mm Common User Bolometer Array (SCUBA) observations (Hughes et al. 1998; Smail et al. 2002; review by Blain et al. 2002). The median redshift for SCUBA sources (SMG) in the HDF(N) with optical counterparts is at least 2. SMG have a typical SFR of $1000\text{--}2000 M_{\odot} \text{ yr}^{-1}$, an order of magnitude greater than in the most active local ULIRGs such as Arp 220 (SFR $50\text{--}150 M_{\odot} \text{ yr}^{-1}$). The FIR intensity is well-correlated with radio emission (on scales greater than a few tens of pc) (Condon 1992; Yun et al. 2001). Elbaz et al. (2002), Garrett (2002) and Chapman et al. (2005) have shown that the relationship is valid out to at least $z \sim 3$.

Star formation dominates the rest-frame MIR and FIR output even if an AGN is present (Downes & Solomon 1998; Frayer et al. 1998) as emission due to dust heating by AGN declines steeply from the NIR to the FIR (e.g. Markarian 231, Soifer et al. 2000). The observed ratio of X-ray to rest frame FIR luminosity is $\lesssim 10\%$ in local active galaxies even when a strong AGN is present and lower still at high redshifts, especially for starburst-dominated sources (Alexander et al. 2003a, 2005a).

Almost half of the optical spectra available for 2-Ms X-ray sources in the HDF(N) indicate the presence of star formation in the same galaxy (Sadler et al. 2002; Barger et al. 2005). There is evidence that radio and X-ray emission has a common origin in star-forming galaxies at relatively low redshifts (Alexander et al. 2002). Bauer et al. (2002b) derive a relationship between radio and X-ray luminosities for 102 emission-line galaxies at $z \leq 1.3$ (of which only 2 sources at $z > 1$ were detected in both radio and X-ray in the data then available):

$$\log L_X = (0.935 \pm 0.073) \log L_R + (13.141 \pm 1.650) \quad (1)$$

where L_X and L_R are the X-ray and radio rest-frame luminosities in W and W Hz^{-1} . This does not seem to hold so well for samples extending to higher redshift; Barger et al. (2007) find no correlation between radio and X-ray luminosities for optically-classified star-forming galaxies in the HDF(N) brighter than $60 \mu\text{Jy}$.

In this paper, we investigate whether the relationship holds at high redshift using classifications independent of optical detections and we explore the properties of radio counterparts to the obscured AGN (type-II AGN) identified from their hard X-ray

photon indices and high X-ray luminosities by Padovani et al. (2004).

Many investigations of high-redshift star formation deliberately exclude AGN hosts. We do not need to do this because we use sub-arcsec resolution to distinguish between different energy sources in the same galaxy, which may correspond to different classifications in different wavelength regimes. The whole field has only been well-resolved by the *HST* and by MERLIN+VLA at 1.4 GHz. The extent of radio emission from high-redshift galaxies in the HDF(N) is typically $1''\text{--}2''$.

We present the first detailed comparison between the highest sensitivity MERLIN+VLA and *Chandra* data ever taken and the *HST ACS* images. The data used in this paper are described in more detail in Section 2, followed by a summary of the Virtual Observatory and RadioNet² software which has made these results possible, in Section 3.1. In Sections 4 and 5 we explain how we derive the radio and X-ray luminosities³ and deduce the origins of the emission, based primarily radio data for the radio sources and X-ray data for X-ray sources. Their relationships are explored in Section 6 and we present evidence for the presence of embedded type-II AGN in radio starbursts in Section 7. We demonstrate statistically the presence of faint radio emission associated with the majority of X-ray sources in Section 8 and summarise our conclusions in Section 9.

2. HDF(N) Data, Cross-Identifications and Redshifts

In this Section we introduce the radio observations and describe briefly the X-ray and other data and tools used to make comparisons. The positions, flux densities and spectral and photon indices of radio sources with X-ray counterparts are listed in Table 1, along with their redshifts and any IR or sub-mm detections. All positions given in this paper have been aligned with the VLA or MERLIN+VLA data as these provide the most accurate reference frame, aligned with the International Celestial Reference Frame (ICRF) to better than 15 milli-arcsec (mas) (Muxlow et al. 2005).

2.1. Radio observations of the HDF(N)

Muxlow et al. (2005), Richards (2000) and Richards et al. (1998) describe the MERLIN and VLA observations of the HDF(N) made in 1996-7. The VLA-only 1.4-GHz image contains 92 sources above its completeness limit of $40 \mu\text{Jy}$ per $2''$ beam ($\sim 5.5\sigma$) in a box of side $10'$ (the 10-arcmin field), the 'radio-bright' sample. The MERLIN field was centred on Right Ascension $12^{\text{h}} 36^{\text{m}} 49^{\text{s}}.4000$, Declination $+62^{\circ} 12' 58''.000$ (J2000), hereafter taken as the reference position.

2.1.1. 1.4 GHz MERLIN+VLA observations and other radio data

The combined MERLIN+VLA 1.4 GHz data reach an rms noise level of $1\sigma \sim 3.5 \mu\text{Jy}$ at $\lesssim 5'$ from the pointing centre, twice the sensitivity of the VLA-only data. Both arrays observed in wide-field mode, using short integration times and multiple narrow frequency channels across the bandpass in order to ensure that time-averaging and chromatic aberrations were less significant than the fundamental limitations of the primary beams. This is

² <http://www.radionet-eu.org/>

³ We assume an empty Friedmann universe ($\Omega_0 = 0$), for consistency with Padovani et al. (2004) and take $H_0 = 70 \text{ km s}^{-1} \text{ Mpc}^{-1}$.

described in detail by Richards (2000) (his section 3.2 and figure 3) and Muxlow et al. (2005) (their section 2). Computational limitations meant that the calibrated MERLIN and VLA data were separately Fourier transformed into multiple small dirty maps covering the region to be imaged; each pair was then combined and CLEANED. Tests showed that, for an image with the same weighting and CLEANING, there was no appreciable difference between this method and data combination in the visibility plane (Muxlow et al. 2005, their figure 1). The final combined images show $\lesssim 6\%$ loss of flux at $5''$ from the pointing centre and there is no systematic radial distortion of the source contours (Muxlow et al. 2005, their figure C1).

Muxlow et al. (2005) resolved all 92 radio-bright sources at $0''.2\text{--}2''$ resolution, see Table 1, Fig. 1 and Muxlow et al. (2005). J123644+621133 is an FR 1 (Fanaroff & Riley 1974) radio galaxy with jets extending over $12''$. Excluding this source, the mean angular size of sources at $z \lesssim 2$ is $1''.3$, corresponding to ~ 10 kpc at $z > 0.8$. Sources at $2 \lesssim z \lesssim 3$ have a mean size of 8 kpc and the source at $z = 4.424$ has a size of 2 kpc. The smaller apparent size of higher redshift sources is probably at least partly due to the non-detection of fainter extended emission (as well as being affected by the adopted cosmology) and is not obviously linked to the inverse relationship between angular size and redshift established for bright radio galaxies by Barthel & Miley (1988).

VLA observations at 8.4 GHz covered the inner HDF(N) to a radius of $\sim 4'$ (Richards et al. 1998; Fomalont et al. 2002) at a resolution of $3''.5$, finding a total of 50 sources within the 10-arcmin field. 27 of these sources were detected at $> 40 \mu\text{Jy}$ by MERLIN+VLA at 1.4 GHz. The remainder cannot be classified using their radio morphologies and are omitted from our analysis, apart from 7 which do have X-ray counterparts, (Section 2.2). We refer to these as 8.4-GHz selected sources. Their properties are given in Table 1, including 1.4-GHz flux densities taken from Richards et al. (1998) where available or calculated using the spectral indices described in Section 2.1.2, so that the rest-frame luminosities of the whole sample can be derived consistently in Section 4.1.

We use S_R to denote the total radio flux density measured by the VLA at either frequency, further subscripted by the specific frequency only where relevant.

Four of the 92 sources were detected at (4 – 20)-mas resolution by the EVN (European VLBI Network) and global VLBI (Garrett et al. 2001; Chi et al. 2006). At the other extreme, the Westerbork Synthesis Radio Telescope at $15''$ resolution detected $\sim 10\%$ more sources than the VLA (Garrett et al. 2000). Further VLA images on larger scales are in preparation (Morrison et al. 2006) and recent low-frequency observations have been made using the GMRT (Lal, D. V., in prep).

2.1.2. Radio spectral indices

The radio spectral index α is given by

$$S_R \propto \nu^{-\alpha}. \quad (2)$$

Asymmetric uncertainties are represented by e.g. $\alpha_{-\sigma_{\alpha_-}}^{+\sigma_{\alpha_+}}$. Richards (2000) and Richards et al. (1998) provide spectral indices and uncertainties for sources detected by the VLA at both frequencies. If sources within the overlapping spatial region were detected at 1.4 (8.4) GHz only, α is a lower (upper) limit depending on the local noise in the 8.4 (1.4) GHz field.

In the case of a 1.4-GHz-only detection σ_{α_-} is approximated as twice the error due to the 1.4 GHz detection,

$$\sigma_{\alpha_-} = \frac{2}{\ln[8.4/1.4]} \frac{\sigma_{S_{R1.4}}}{S_{R1.4}} \quad (3)$$

and σ_{α_+} is given by an analogous expression for 8.4-GHz-only detections.

Radio sources classified as AGN or as starbursts (see Section 5) detected at both frequencies had spectral indices in the ranges $(-0.4 < \alpha < 1.4)$ and $(0.3 < \alpha < 1.7)$ respectively; all unclassified sources had α within the extrema of these ranges. Where α is a lower limit we set σ_{α_+} to the relevant upper limit. e.g. $(1.7 - \alpha)$ for starburst or unclassified sources. The errors in α for 8.4-GHz selected sources were deduced in a similar fashion for the opposite limits. For sources outside the 8.4 GHz field we adopted typical values of α of 0 and 0.8 for AGN and starbursts respectively and an average of 0.4 for unclassified sources, using the extrema to deduce the uncertainties, so that for example a starburst would have $\alpha = 0.8_{-0.5}^{+0.9}$.

2.2. X-ray data

The *Chandra* X-ray observatory made a total of 2 Ms multi-band exposures of the HDF(N) (Alexander et al. 2003b). All X-ray flux densities, counts and luminosities given in this paper refer to the *Chandra* full band from 0.5–8.0 keV unless otherwise stated. Soft-band values are used for J123709+620841 and J123646+621445 as they were not detected in the full band. There are 100 sources in common within the area of overlap between the whole VLA and *Chandra* fields of view, with a median offset of $\sim 0''.2$ after small corrections to align the X-ray frame (Alexander et al. 2003b).

2.2.1. X-ray – radio counterparts

The *Chandra* observations completely enclose the radio 10-arcmin field and the decline in sensitivity in both images towards the edges of this region is less than 6%. This field contains 253 X-ray sources with position uncertainties $0''.3\text{--}0''.9$. Fifty-five (60%) of the radio-bright sources have X-ray counterparts within $0''.9$ of the radio peak; the separation is $< 0''.4$ for 42 of these. Increasing the cross-match search radius up to $2''$ failed to produce any more matches. One or two additional matches appear for each additional arcsec radius from $2\text{--}5''$. Each of these radio sources also has a counterpart at $< 0''.9$; in about half these cases the multiple associations appear to be genuine (e.g. similar redshifts). We consider that we can only be confident that the emission is coming from the same galaxy for the 55 unambiguous matches at $< 0''.9$ separation. These make up 22% of the X-ray detections in the 10-arcmin field. Seven additional 8.4-GHz selected sources have X-ray counterparts within their combined position uncertainties.

We compared the largest angular size of each radio-bright source with the X-ray – radio source separation, represented by the solid circles in Fig. 1 (J123644+621133, with an angular size of $12''$, has been omitted). In every case the X-ray peak is no further from the radio peak than the most extended radio emission. We produced randomised X-ray position errors, in a Gaussian distribution, such that 80-90% of the X-ray positions were within the published errors of $0''.3\text{--}0''.9$ (Alexander et al. 2003b), which are plotted as hollow squares. The radio peak position errors are negligible in comparison ($\lesssim 0''.1$). There is no evidence for any systematic excess in the measured source separations with re-

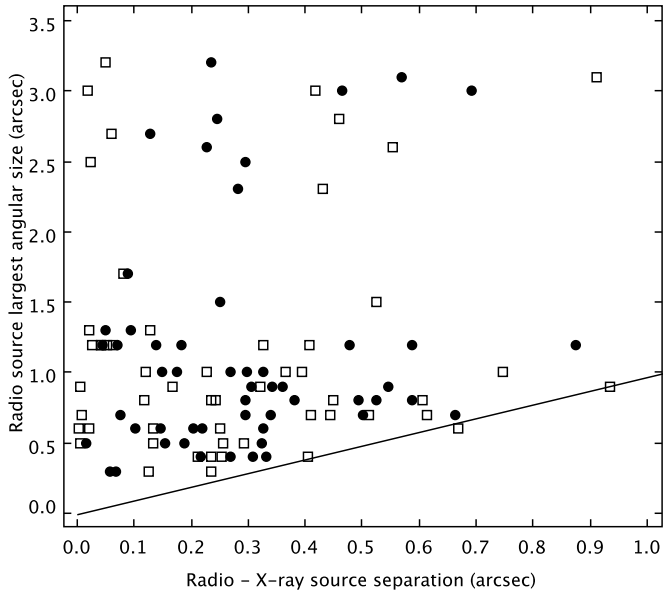


Fig. 1. The filled symbols show the measured angular sizes of radio sources with X-ray counterparts compared with the radio-X-ray peak separation. The sloping line has a gradient of unity, showing that all the radio sources have an angular size greater than the distance to their X-ray counterpart. The hollow symbols show the measured angular size as a function of randomised X-ray position errors (see text).

spect to the X-ray position errors but peak offsets of $\lesssim 1''$ cannot be ruled out.

2.2.2. X-ray photon indices

The X-ray photon index Γ , for flux density F_X in $10^{-18} \text{ W m}^{-2}$ at energy E keV is defined by

$$F_X(E) \propto E^{-\Gamma} \quad (4)$$

and Γ is equivalent to $\alpha + 1$ (where α is the spectral index). All values measured by Alexander et al. (2003b) lie in the range $-1 \lesssim \Gamma \lesssim 2$, who give upper and lower bounds to the uncertainty, $\sigma_{\Gamma+}$ and $\sigma_{\Gamma-}$ only for sources detected in more than one sub-band. If a source is only detected in the full and soft bands then Γ is a lower limit so we take $\sigma_{\Gamma+} = 2 - \Gamma$ and approximate $\sigma_{\Gamma-}$ as twice the error due to the uncertainty in the soft band counts. If a source is only detected in the full and hard bands then Γ is an upper limit so we take $\sigma_{\Gamma-} = \Gamma - (-1)$ and approximate $\sigma_{\Gamma+}$ as twice the error due to the uncertainty in the hard band counts. If sources were only detected in the full band, Alexander et al. (2003b) give an estimated value of $\Gamma = 1.4$ and we adopt $\sigma_{\Gamma-} = \sigma_{\Gamma+} = 0.6$. In all cases we constrain $\sigma_{\Gamma-} \leq 0.6$ in order to avoid non-physical negative limits on L_X (see Section 4.2).

2.3. Hubble Space Telescope observations

The original HDF and surrounding fields (out to a distance of $\sim 5'$) was observed by the *HST* *WFPC2* in 1996 (Williams et al. 1996). In 2003 the GOODS project used the *HST* *ACS* to re-observe the HDF region in the F435W, F606W, F775W and F850LP filters (*B*, *V*, *i* and *z* bands). We find that the GOODS images and source catalogue r1.1z (Giavalisco et al. 2004) require a linear shift of $-0'.342$ in Declination to align them with the ICRF.

2.4. IR and sub-mm sources

The *ISO* fields and the *Spitzer* catalogue published by Teplitz et al. (2005) only cover part of the 10-arcmin field so it is only possible to give meaningful statistics for the fractions of the IR catalogues detected at other wavelengths (not visa versa). More quantitative analysis will be available using further *Spitzer* results at $24 \mu\text{m}$ (see e.g. Beswick et al. 2006). Extensive SCUBA searches have been made over most of the HDF(N).

2.4.1. Mid-infrared detections

One hundred sources were detected in the inner HDF(N) by *ISO* at 7 or $15 \mu\text{m}$ (Aussel et al. 1999). Although the beam size was $3-6''$ the tight correlation between radio and $15 \mu\text{m}$ flux densities out to at least $z = 3$ (Garrett 2002, Elbaz et al. 2002, see Section 1) supports the association of radio and IR sources within the position errors even if they overlap more than one optical source. 28 radio-bright sources lie within the *ISO* field, of which 17 have *ISO* counterparts (Muxlow et al. 2005). All matched sources were detected at $15\text{-}\mu\text{m}$ except for J123656+621301. This is nonetheless an extended diffuse radio source with a very steep spectrum characteristic of a starburst. An additional $7\text{-}\mu\text{m}$ source in the catalogue of Goldschmidt et al. (1997) is matched with the FR 1 J12364+621133.

The radio-MIR association has been reinforced by recently-published *Spitzer* observations at $16 \mu\text{m}$ (Teplitz et al. 2005). 18 *Spitzer* sources have MERLIN+VLA counterparts within $1''.2$. Half of these lie outside the *ISO* fields. Of the other nine, 7 already had *ISO* counterparts (including the very red source J123651+621221 at $z = 2.71$; Teplitz et al. (2005) associate the IR emission with an elliptical galaxy at a similar separation but lower redshift). The other two, J123633+621005 and J123708+621056, lie close to the edges of the *ISO* field where its noise was higher. We cannot confidently associate J123646+621445 with the *Spitzer* source $1''.7$ to the SW as they have two separate optical counterparts. An *ISO* source lies within $3''$ of the $16 \mu\text{m}$ source but further from J123646+621445. There are no further candidate radio-IR matches within $2''$.

The combined *Spitzer* and *ISO* data contain 205 separate 15 - or $16\text{-}\mu\text{m}$ sources within the 10-arcmin field of which a quarter (53) have X-ray counterparts. Even fewer (26, 13%) have radio-bright counterparts, but almost all of these (21/26) are also X-ray detections. This complements the tendency, noted by Alexander et al. (2002), that optically identified (emission line) $15 \mu\text{m}$ starbursts with X-ray emission are more likely to have radio counterparts than those without. Four of the 7 8.4-GHz selected sources with X-ray counterparts have *ISO* counterparts, 3 of which were also detected by *Spitzer*.

2.4.2. SCUBA detections

Several sets of observing and data reduction techniques have produced various SCUBA catalogues optimised for different regions and properties (e.g. Serjeant et al. 2003; Borys et al. 2004; Wang et al. 2004; Chapman et al. 2005). The techniques used to minimise ambiguity in cross-identifications are summarised in Muxlow et al. (2005). The most comprehensive list is currently provided by Borys et al. (2004) (the revisions by Pope et al. (2005) do not affect any radio-bright sources). We use all their secure identifications between SMGs and radio-bright sources. We also include the additional identifications of J123622+621629 and J123711+621325 made by Chapman et al. (2005). We do not include the SMGs known as HDF 850-1 and

850-6 as most authors conclude that they do not have radio-bright counterparts. J123608+621431 is $\sim 3''$ from the nearest X-ray source so it is not included in the detailed analysis in this paper, but both objects are within the larger error circle of a SCUBA source. We reject the identification of J123646+621445 for reasons similar to those given in Section 2.4.1 with respect to IR sources.

This leaves 16 radio-bright sources in the 10-arcmin field with SCUBA counterparts, of which 11 were also detected by *Chandra*; one further 8.4-GHz source has both SCUBA and X-ray detections. All these sources have either spectroscopic or photometric redshifts, which we adopt in preference to redshifts derived from the 1.4-GHz/850- μ m flux density ratio in order to avoid circular arguments.

2.5. Redshifts

61 radio-bright sources and 140 *Chandra* sources in the 10-arcmin field have measured redshifts, including 50 of the 55 radio-bright X-ray sources. 19 of the 8.4-GHz selected sources also have measured redshifts, including 7 with X-ray counterparts.

Table 1 gives our adopted redshift measurements, uncertainties σ_z and references for the sources detected in both regimes. We include the published errors, σ_z , where given. If not we adopt $\sigma_z = 0.003$ for spectroscopic redshifts, which were all obtained using the Keck LRIS or instruments with resolution as good or better. The uncertainties in photometric redshifts are $\leq z/4$ apart from J123725+621128 where $1 < z < 2$ was estimated from the K/z band flux density ratio (Hornschemeier et al. 2001). The uncertainties do not include possible misidentifications of objects or of spectral lines, nor instabilities in photometric fitting. In most cases the differences between different redshift estimates for the same source are small, or have been discussed and resolved in the literature. The redshift for J123616+621513 has now been revised to 2.58 (Chapman et al. 2004a). We adopt recently-published redshifts for faint *NICMOS* or *ACS* galaxies associated with the radio sources J123606+621021, J123642+62133, J123651+621221 and J123716+621512, in preference to the photometric redshifts derived by Barger et al. (2003) for their X-ray counterparts using more widely separated, older optical detections.

The redshift distributions of radio and X-ray sources and of objects detected in both regimes are compared in Fig. 2. All three distributions peak at $0.5 < z < 1.0$ but the fraction of X-ray sources with measured redshifts which are radio-loud changes from less than a third at $z < 1$ to a half or greater at higher z . A similar increase in codetections with redshift is seen in the fraction of radio sources which are X-ray-selected type-II AGN. We used the Kolmogorov-Smirnov test to investigate the relationship between the redshift distributions of the radio and X-ray sources. We found that there is a 93% probability that radio and X-ray sources at $z < 1.1$ are drawn from the same population and a 98% probability for sources at $z > 1.1$, but this drops to an insignificant probability of 27% for all redshifts considered together. This only makes sense if the radio counterparts to X-ray sources at lower redshifts are a separate population from those at higher redshifts. These implications are discussed in Sections 5.2 and 7.

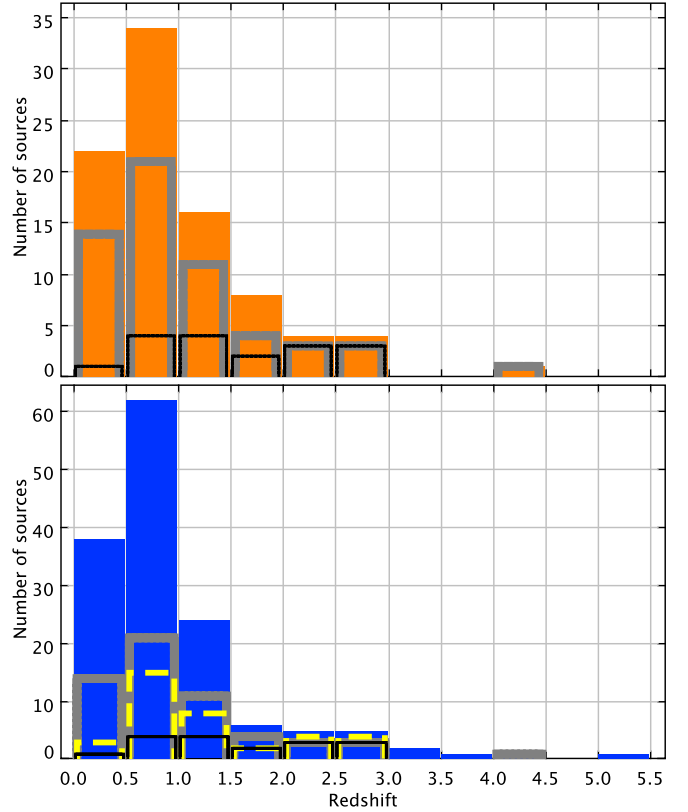


Fig. 2. The distribution of sources with published redshifts in the 10-arcmin field. The filled blue area in the lower panel shows X-ray sources and the dashed yellow line shows X-ray selected type-II AGN. The filled orange area in the upper panel shows radio sources. In both panels the cross-matched X-ray and radio sources, and those which are also X-ray selected type-II AGN, are shown by the thick grey and thin black lines, respectively.

3. New Technology

3.1. Virtual Observatory facilities

We made use of a wide range of published surveys and catalogues. These were obtained using the VizieR⁴ service where possible, in order to select sources in the exact area covered by the radio data, and obtain tables in VOTable⁵ format for ease of further manipulation. Other data (e.g. in IPAC format) were converted to VOTable using TopCat⁶, which preserves accuracy equivalent to full double precision. Sources were crossmatched using either the AstroGrid⁷ Xmatch tool or TopCat, which allowed us to identify and correct for any systematic linear offsets due to astrometric errors. We also used TopCat to calculate luminosities and other derived quantities (Section 4) presented in the tables, and to prepare many of the plots.

The original images have resolutions from $\sim 0''.015$ (*HST*) to several arcsec (*ISO*, *SCUBA*). The MERLIN+VLA and *HST* maps are made up of many small panels each containing about a million pixels. We used the Aladin visualisation tool as modified for the Euro-VO⁸ to find, cross-identify and visualise regions of interest on such different scales; an example is shown

⁴ <http://vizier.u-strasbg.fr/>

⁵ <http://cdsweb.u-strasbg.fr/doc/VOTable/>

⁶ <http://www.starlink.ac.uk/topcat>

⁷ <http://www.astrogrid.org>

⁸ <http://www.euro-vo.org>

in Fig. 3. The International Virtual Observatory⁹ Simple Image Access Protocol (SIAP) for descriptions of images and their locations is used to locate the corresponding fields in *Chandra*, MERLIN+VLA and *HST* images despite the different resolutions, image sizes and even orientations. The PLASTIC¹⁰ protocol developed for VOTech¹¹ allows any of these VO tools to manipulate the same data.

3.2. RadioNet tools and dynamic radio imaging

It is now feasible to image much larger radio fields in entirety, compared with the epoch when the MERLIN+VLA observations were made, thanks to increased computing power, improved algorithms in AIPS and the use of Virtual Observatory standards and tools for data management. We made 81 slightly overlapping square images, each of $1024 \times 0'.0625$ pixels on a side. We combined these images into a single (8×8) arcmin² 1.4-GHz image, hereafter the 8-arcmin field. This contains over 67 Mpixels, covering most of the maximum sensitivity regions of both the radio and X-ray images, with good overlap with the ACS data. This will be extended to cover the 5-arcmin radius region of near-optimum radio sensitivity. We describe our use of the new 8-arcmin HDF(N) image in Section 8.

The range of baseline lengths in the combined MERLIN+VLA data means that maps can be extracted at resolutions of $0'.2-2''$ depending on whether the observer wants to investigate potential compact hot spots or faint extended emission. Muxlow et al. (2005) gives a full description of the method which was used to produce the earlier hand-processed images. We now provide an automatic imaging service which extracts the required region and convolves it with the chosen restoring beam within this resolution range. This uses the python-based package ParselTongue¹² (Kettenis et al. 2006), developed in the RadioNet Consortium, to provide a scripting interface between AstroGrid and ‘classic’ AIPS. The AstroGrid workbench offers a simple dialogue box for the user to select image size, resolution and region within the HDF(N). These parameters are passed to the MERLIN archive server which uses ParselTongue to extract the required image. A pointer to the image and a basic (SIAP-compliant) description is either returned straight to the user or can be used to pass it to another VO-enabled tool such as Aladin or a source extractor. This VO tool and the complementary MERLINImager (which operates on the visibility data for other MERLIN archive data) are the first to allow an astronomer to obtain customised radio images without having to install their own specialised radio data reduction package. Moreover, only the required image (at most 0.25 GB) is moved over the internet to the point of use; the parent data set, which can be many GB, is processed in situ.

4. Estimation of radio and X-ray luminosities

There is no correlation between radio and X-ray flux densities for the whole cross-matched sample nor for any subsets; however this is not surprising given the wide span of redshifts and the different behaviour of the spectral/photon indices for different sources. We therefore compared the *K*-corrected luminosities for all 50 sources with measured redshifts.

4.1. Rest frame 1.4-GHz radio luminosity

Table 1 lists the observed-frame 1.4-GHz total radio flux density per source, S_R , in μJy . The flux densities and their uncertainties (σ_{S_R}) are given in Muxlow et al. (2005) and Richards et al. (1998).

We assume an empty Friedmann universe ($\Omega_0 = 0$), for consistency with Padovani et al. (2004) and take $H_0 = 70 \text{ km s}^{-1} \text{ Mpc}^{-1}$. The radio rest-frame luminosity L_R , taking into account the *K*-correction and the expansion of the bandwidth in the observed frame, is given in W Hz^{-1} by

$$L_R = \frac{S_R}{10^{32}} 4\pi(d \times 3.086 \times 10^{22})^2 (1+z)^{\alpha-1} \quad (5)$$

where d is the luminosity distance in kpc, given by

$$d = \frac{cz}{H_0} (1+z/2) \quad (6)$$

where the speed of light, c , is in km s^{-1} . The lower bound on the uncertainty σ_{L_R-} is given by

$$\sigma_{L_R-} = \sqrt{\sigma_{L_R(\alpha-)}^2 + \sigma_{L_R(S_R)}^2 + \sigma_{L_R(z)}^2} \quad (7)$$

where the partial errors in L_R due to the lower bound on the spectral index error, due to the flux density error and due to the redshift error are given by:

$$\sigma_{L_R(\alpha-)} = L_R \sigma_{\alpha-} \ln(1+z) \quad (8)$$

$$\sigma_{L_R(S_R)} = L_R \frac{\sigma_{S_R}}{S_R} \quad (9)$$

$$\sigma_{L_R(z)} = L_R \sigma_z \left(\frac{2(1+z)}{z(1+z/2)} + \frac{\alpha-1}{1+z} \right). \quad (10)$$

Substituting $\sigma_{\alpha+}$ for $\sigma_{\alpha-}$ in Equation 8 gives $\sigma_{L_R(\alpha+)}$ which then replaces $\sigma_{L_R(\alpha-)}$ in Equation 7 to give the upper bound to the uncertainty in L_R , σ_{L_R+} . Table 2 gives L_R and its upper and lower bounds ($L_R - \sigma_{L_R-}$ and $L_R + \sigma_{L_R+}$).

4.2. Rest-frame 0.5-8.0 keV X-ray luminosity

The rest-frame X-ray luminosity is given by the analogy of Equation 5.

$$L_X = \frac{F_X}{10^{18}} 4\pi(d \times 3.086 \times 10^{22})^2 (1+z)^{\Gamma-2} \quad (11)$$

The observed flux densities are given in Table 1, taken from Alexander et al. (2003b). This does not give flux density uncertainties so we assume that the relative uncertainty in the flux density is equivalent to the relative uncertainty in the counts (C). σ_{C-} and σ_{C+} are the lower and upper bounds on the uncertainties in the counts. The lower limit to the luminosity uncertainty σ_{L_X-} is given by the sum in quadrature of uncertainties due to the lower limits to the errors in Γ and F_X and to the error in z

$$\sigma_{L_X(\Gamma-)} = L_X \sigma_{\Gamma-} \ln(1+z) \quad (12)$$

$$\sigma_{L_X(F_X-)} = L_X \frac{\sigma_{C-}}{C} \quad (13)$$

$$\sigma_{L_X(z)} = L_X \sigma_z \left(\frac{2(1+z)}{z(1+z/2)} + \frac{\Gamma-2}{1+z} \right) \quad (14)$$

and the upper limit to the uncertainty, σ_{L_X+} , is given by an analogous expression. Table 2 gives L_X and its upper and lower bounds ($L_X - \sigma_{L_X-}$ and $L_X + \sigma_{L_X+}$).

⁹ <http://www.ivoa.net>

¹⁰ <http://plastic.sourceforge.net/>

¹¹ <http://eurovotech.org/>

¹² <http://www.radionet-eu.org/rnwiki/ParselTongue>

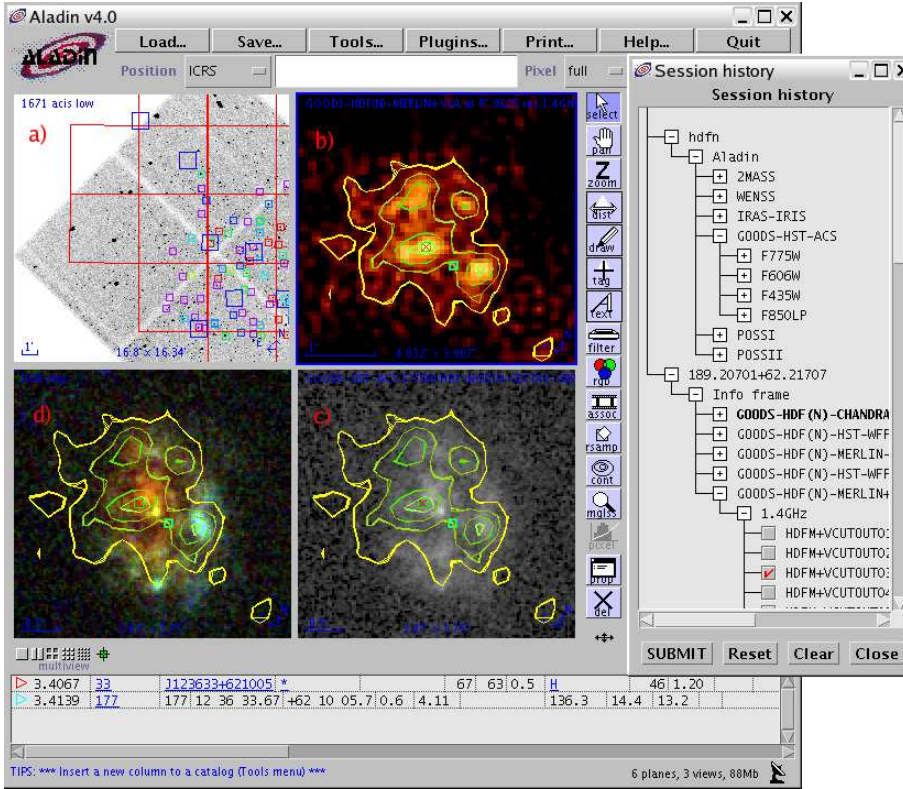


Fig. 3. The use of the Euro-VO Aladin and PLASTIC to investigate the starburst candidate J123633+621005. Clockwise from top left, the panels show: a) *Chandra* image overlaid with the outlines of *HST ACS* field boundaries; clicking in the appropriate square selects the relevant image(s) for loading. The coloured symbols show radio sources, with symbol size proportional to source size and shade proportional to redshift. b) Radio contours for J123633+621005; the red cross and blue square mark radio and X-ray peaks, respectively. c) *ACS* F775W image d) *ACS* false colour composite of F435W, F606W and F850LP bands, all overlaid with radio contours. The scale bars in the bottom left of each panel represent a) 1 arcmin, b) 1 arcsec, c) and d) 0".5.

5. Origins of Radio and X-ray emission

In this Section, we discuss diagnostics for the specific origins of the radio and X-ray emission, based on the references and discussion of Section 1, applied to the derived source properties. We keep the initial radio source classification independent of X-ray properties (and vice versa) as we wish to investigate whether the observed radio and X-ray emission comes from different sources within the same galaxies. In particular, we do not use published radio-X-ray relationships such as Equation 1 for classification, but compare our results with this in the next Section, 6.

5.1. The nature of the radio emission

The main diagnostics for the origins of the radio-bright emission are:

1. **Morphology** The presence of a bright, compact core or clear radio jets/lobes suggests the presence of a radio AGN. Extended emission (kpc scales) with no obvious peaks or jets/lobes is more likely to originate from star formation.
2. **Spectral Index** Radio emission with $\alpha \lesssim 0.4$ is likely to be powered by an AGN. Steeper-spectrum emission is usually of starburst origin but could indicate a lobe-dominated AGN system, hence the need to inspect the structure.
3. **The Radio-FIR link** Rest-frame FIR or MIR emission bright enough to be detectable in the HDF(N) (including by SCUBA, for high- z sources) indicates a ULIRG-like intensity or greater, very likely to be of starburst origin, found to be closely correlated with radio emission. Even when there is separate evidence for the presence of an AGN (see Section 1), rest-frame MIR emission at or greater than ULIRG-like luminosity is far in excess of the predictions of any known AGN model (Alexander et al. 2005a, see also Section 7.2) and AGN are unlikely to be responsible

for more than 20% of the bolometric luminosity (Alexander et al. 2003a, 2005b).

4. **Optical appearance** If bright radio and optical galaxy cores coincide, this is further evidence for the presence of an AGN. Extended radio emission outside the apparent optical extent of a galaxy is likely to be of jet origin. On the other hand, extended radio emission within the optical galaxy, especially if associated with bright optical knots, indicates active star formation. Very disturbed or interacting galaxies with associated diffuse radio emission provide supporting evidence of conditions for starburst activity. As explained in Section 1, obscuration can hide optical signatures, especially in starbursts, so absence of (optical) evidence is not conclusive evidence of absence of a particular radio emission mechanism.

Muxlow et al. (2005) described in detail the application of these criteria in classifying radio sources as Starburst (SB), Active Galactic Nucleus (AGN), or unclassified (U). Note that the AGN status covers any emission powered by an AGN, whether it arises from accretion or from jets/lobes. Using the MERLIN+VLA data, we are able to distinguish between extended lobes and cores, but not between pc-scale jets and the core itself, although the resolved emission of AGN origin must be from jets or lobes. The presence of two unambiguous FR 1 in the HDF(N) already represents a greater space density than would be expected from local number counts (Snellen & Best 2001), making it unlikely that a high proportion of the unidentified extended or steep-spectrum sources have large radio lobes.

VLBI results support the AGN interpretation of compact, flat-spectrum radio cores. Extremely compact radio cores (brightness temperature $> 10^5 - 10^6$ K) were detected in J123642+621331, J123644+621133, J123646+621404 and J123652+121444 using the European VLBI Network (EVN) and global VLBI (Garrett et al. 2001; Chi et al. 2006), confirming the presence of an AGN. J123644+621133 is unmistakably an FR 1. The EVN recovers all the VLA flux from J123646+621404.

About 1/3 of the VLA flux from J123652+121444 is present in the 4-mas resolution global VLBI image but the source is known to be variable (Richards et al. 1998). All three sources have flat or inverted spectra. J123642+621133 is discussed in more detail in Section 5.3; in summary we infer that it consists of compact AGN-powered emission embedded in a more diffuse starburst. The MERLIN+VLA data suggest that this is also the situation for J123635+621424 and J123642+121545.

Table 2 gives our classifications for the objects with X-ray counterparts. The recent ACS and *Spitzer* data and improved SCUBA source lists have allowed us to strengthen the classification of a number of sources. We have changed the classification of 4 sources, as follows. J123622+621544 was tentatively assigned AGN status by Muxlow et al. (2005) but the ACS image shows that the radio emission is extended over bright optical knots in a distorted spiral, not seen in the original CFHT plate (Canada-France-Hawaii Telescope, Barger et al. 1999). It is also a new MIR detection by *Spitzer* and has a radio spectral index > 0.6 so we reclassify J123622+621544 as a starburst. We infer from the *Spitzer* and ACS images that two previously unclassified sources with steep radio spectra are starbursts. J123629+621046 is extended, with a red optical counterpart which is either a distorted galaxy with a dust lane or two interacting galaxies. J123641+620948 has a compact core but the ACS image confirms the suggestion by Cohen et al. (2000) that it is associated with two interacting spiral galaxies. The ACS morphology allows us to reclassify J123642+621545 as a starburst candidate with a possible AGN core, as its extended radio emission overlays blue knots in the arms of a face-on spiral. It also possesses a relatively bright compact radio and optical core. It was detected by *ISO* and has an intermediate radio spectral index of 0.5.

Note that the classifications of radio-bright sources are made primarily on the basis of radio properties such as morphology and/or spectral index (conditions 1. and 2. above) whilst information from other wavebands (conditions 3. and 4.) is used as supporting evidence. The origins of the radio emission from the seven 8.4-GHz-selected sources with X-ray counterparts are less certain as they are unresolved in the radio and have approximate spectral indices or upper limits only. The ACS images show that J123637+621135, J123639+621249 and J123648+621427 are associated with spiral galaxies with knots of star-formation (the lower-resolution CFHT image of J123648+621427 appeared elliptical). J123644+621249 is associated with a pair of apparently interacting optical galaxies at very similar redshifts. All four have $\alpha \gtrsim 0.6$ and we list them as starbursts although the closest (J123637+621135) is in fact of low luminosity, more like a normal star-forming galaxy. The remaining 3 have flatter spectra; J123655+621311 is associated with an elliptical galaxy likely to contain an AGN; the other two are unclassified.

In total, the 92 radio-bright sources include 23 unclassified objects, 52 starbursts and 17 AGN, using the radio-based classification. The 55 sources with X-ray counterparts include 9 of the unclassified sources, 36 starbursts and 12 radio AGN. The starburst:AGN ratio is almost identical, $\approx 3 : 1$, to the that of the full radio-bright sample. The three starbursts which contain radio AGN (counted once only, as starbursts) are all X-ray detections. MIR observations only cover part of the field but contain 22 sources detected at 15- or 16- μm as well as in the radio and X-ray. Nineteen of these (86%) are radio starbursts, including 3 with radio AGN cores, 4 with X-ray selected type-II AGN (see Section 5.2) and one with both. Two more are probably AGN, J123646+621404 (also an X-ray type-II AGN) and J123709+620841 (see Muxlow et al. 2005). J123655+620808

is unclassified as, although the ACS image shows an apparently spiral galaxy with a dust lane, the extended radio emission is misaligned.

5.2. Origins of X-ray emission

The great majority of X-ray sources in the HDF region are unresolved by *Chandra* so only luminosity and spectral index information may be available to determine the specific origin of the X-ray emission. Many classifications in the literature are based on optical and other properties which could be due to separate mechanisms within the host galaxy. A comprehensive source-by-source breakdown is not available but out of the 19 sources from the 1 Ms sample cross-matched by Bauer et al. (2002b), about 1/3 are classed as emission-line galaxies and presumed to have X-ray emission of starburst origin; most of the remainder are X-ray AGN.

Star-forming galaxies and ULIRGs show a close correlation between their star formation rates represented by FIR emission, and both hard- and soft-band X-ray emission (Ranalli et al. 2003), although Rosa-Gonzalez et al. (2007) has recently found that, for a higher-redshift sample in the CDF(S), the SFR implied hard-band luminosities can be excessive compared from the rates derived from soft-band or *Spitzer* MIR data, presumably due to obscured-AGN contamination in the hard band. Hard X-ray emission associated with star formation is thought to originate from high-mass X-ray binaries (e.g. Grimm et al. 2003). More slowly-evolving low-mass X-ray binaries are likely to be less significant (Rosa-Gonzalez et al. 2007), especially in young starburst galaxies. This leaves young supernova remnants and hot plasmas associated with star-forming regions and galactic winds as possible sources of the soft-x-ray component (Ranalli et al. 2003), especially if super star clusters are forming (Griffiths et al. 2000), as discussed by Norman et al. (2004).

The X-ray luminosity of most optically classified starbursts is $< 10^{35}$ W (Alexander et al. 2002) whilst the presence of detectable hard band (2–8 keV) emission and X-ray luminosities $\geq 10^{35}$ W is usually taken to indicate the presence of an AGN; $\geq 10^{37}$ W implies a QSO (Alexander et al. 2003a). However, it is not unreasonable that the most extreme starbursts could exceed an X-ray power of 10^{35} W, if the X-ray luminosity is proportional to the rest-frame IR emission (e.g. Ranalli et al. 2003), whilst some nearby FR 1 have X-ray luminosities of only $10^{33} - 10^{35}$ W (Evans et al. 2006). Soft-band dominated X-ray emission (photon index $\Gamma \sim 2$) can indicate a starburst origin (Ptak et al. 1999) but is also seen from unobscured AGN (George et al. 2000). In the latter situation the emission could be due to accretion or to jets but both mechanisms are AGN-powered and included in X-ray AGN statistics.

Obscured (type II) AGN have a harder photon index ($\Gamma \lesssim 1.0$); they are the only known sources with $\Gamma \lesssim 0.5$ (Alexander et al. 2005a) but $0.5 < \Gamma < 1$ is also seen from high-mass X-ray binaries in starbursts. Nonetheless, the combination of $\Gamma \lesssim 1$ with a rest-frame 2–8-keV luminosity $L_{\text{XH}} \geq 10^{35}$ W can only be explained by a type-II AGN (see Section 6.2). Padovani et al. (2004) identified a total of 91 such sources in the HDF(N) with a hardness ratio corresponding approximately to $\Gamma \lesssim 1.15$. Of these, 64 lie within the 10-arcmin field and 17 are radio-bright. These are identified in Table 2. A column density $N_{\text{H}} > 10^{27} \text{ m}^{-2}$ is required to provide sufficient obscuration. The estimates of N_{H} given by Alexander et al. (2005a) for SMG confirmed that all 8 of the type-II AGN common to their sample and ours exceed this threshold.

Bauer et al. (2004) find that around 75–90% of the 2-Ms HDF(N) X-ray sources are AGN, of which about 2/3 appear absorbed, and about half the remainder are starbursts. A variety of studies of the GOODS fields, including the use of multi-wavelength properties (Hornschemeier et al. 2001; Bauer et al. 2002b; Szokoly et al. 2004) give similar results, implying a ratio of approximately 8:1 AGN to starbursts among the X-ray detected sources.

Our sample contains 62 X-ray sources with radio-bright counterparts of which 17 or 18 appear to be heavily obscured X-ray AGN. In total, 37 (about 2/3) of the sources with measured redshifts, have hard-band X-ray luminosities brighter than 10^{35} W (see Section 6.2) suggesting the presence of an AGN of some type (Alexander et al. 2003a; Cowie et al. 2004a). Statistically, the majority of all the X-ray emission is probably AGN-powered but it is not possible to distinguish between very luminous but softer emission from starbursts or unobscured AGN on the basis of X-ray properties alone; moreover, diagnostics from other regimes do not guarantee that the emission is from the same phenomenon on a sub-galactic scale. We therefore concentrate on comparing the X-ray-selected type-II AGN population with radio sources classified as AGN or as starbursts.

5.3. The high-redshift source J123642+121331

The highest redshift radio source, J123642+621331, at $z = 4.424$, has a high total 1.4-GHz flux density (467 μ Jy). It has a steep radio spectrum, it is a very reddened NICMOS detection (Waddington et al. 1999) and it was detected by *ISO* at 15 μ m, all properties consistent with starforming activity. Its 1.4-GHz/FIR ratio, however, is 20–50 times higher than other HDF(N) starforming galaxies (Garrett 2002). The MERLIN+VLA image shows that about 10% of the flux is diffuse and extended at between 100–200 mas from the core (≈ 1 kpc), which is likely to contain the starburst component. The star formation rate inferred from the IR flux density is $\approx 1000 M_{\odot} \text{ yr}^{-1}$, comparable to the other highest star formation rates deduced for starbursts in the HDF(N), which would account for $\approx 1\%$ of the radio emission.

The compact core is AGN-dominated; the EVN detected over half the 1.4-GHz flux (Garrett 2002) and global VLBI (Chi et al. 2006) resolves a jet component a few tens of pc from the core. J123642+621331 has a measured $\Gamma = 1.35$, above the limit for type-II AGN, but Padovani et al. (2004) noted that high-redshift sources might be misclassified. The expressions in Section 4.2 assume that Γ is constant from the observed frame to the rest frame. Alexander et al. (2005a), in their fig. 7, demonstrate how absorption is a strong function of wavelength, such that for $N_{\text{H}} \gtrsim 2 \times 10^{27} \text{ m}^{-2}$, rest-frame energies $\gtrsim 6$ keV are much less affected than lower energies. At $N_{\text{H}} \gtrsim 5 \times 10^{27} \text{ m}^{-2}$ the iron emission and absorption lines, at rest frame energies 6–7 keV and 7–8 keV respectively, become more prominent. The measured Γ is derived from the ratio of flux densities above and below 2 keV in the observed frame. This dividing energy corresponds to $\gtrsim 6$ keV at $z \gtrsim 2$, so the observed Γ of a high redshift absorbed source may appear greater than the actual rest-frame 0.5–8 keV photon index. In turn, the actual L_{X} would be higher than the value given in Table 2. J123642+621331 would be most strongly affected. If it is a type-II AGN with a rest frame 0.5–8 keV $\Gamma \lesssim 1.15$, this is compatible with the observed $\Gamma = 1.35$.

6. Relationships between X-ray and radio luminosities

Figure 4 shows the relationship between L_{R} and L_{X} taken from Table 2 for the radio-bright X-ray sources with redshifts. The symbol sizes and shapes represent the largest angular size and the classification applied to the radio emission with a blue **A** denoting the presence of an X-ray selected type-II AGN. The shade of the symbols indicates the redshift. The accuracy of our estimates of L_{R} and L_{X} and potential selection effects are shown in Fig. 5, for all cross-matched sources with redshifts. All sources shown have measured flux densities in both radio and X-ray regimes and measured redshifts (Section 2.2 and Table 1). Filled triangles pointing up (down) indicate objects which were detected at both 1.4 and 8.4 GHz (in at least two X-ray bands) giving a measured spectral (photon) index. Thus, the filled stars show objects with complete measurements. Where one band is a defined limit, an arrow shows the resulting direction of uncertainty in the luminosity. Open triangles show sources where the spectral or photon index has been estimated as described in Sections 2.1.1 and 2.2. The error bars were derived as described in Section 4 which also describes the method for estimating spectral (photon) indices where a source was only detected in one band in the radio (X-ray) regime; such sources are shown by open triangles pointing up (down).

Sources with a given rest-frame luminosity can be detected at higher redshifts if they have steeper spectra, implying that the sample might be biased towards radio starbursts with low-obscuration X-ray counterparts. The red lines in Fig. 5 show the limits of detectability by the MERLIN+VLA and *Chandra* observations described in Section 2 for the two arbitrary combinations of α and Γ . The lines are marked with the redshifts out to which a source would be detectable for the combination of luminosities at that point and the spectral/photon index combination for that line. This shows that X-ray sources at $z \gtrsim 1.5$ need to have $L_{\text{X}} \gtrsim 10^{35}$ W (i.e. in the AGN regime) to be detectable if they have harder photon indices.

6.1. Relationships for starburst-selected sources

Fig. 6 shows that there is a correlation between L_{X} and L_{R} at lower luminosities but there is a very large scatter at $L_{\text{X}} \gtrsim 10^{35}$ W, in particular for sources at $z \gtrsim 1.3$. We investigated this by looking for power-law relationships between $\log L_{\text{R}}$ and $\log L_{\text{X}}$ expressed as

$$\log L_{\text{X}} = B \log L_{\text{R}} + A \quad (15)$$

using values of the intercept and slope, A_i and B_i such that the derived i th values of $\log L_{\text{Xi}}$ and $\log L_{\text{Ri}}$ enclosed the observed values of $\log L_{\text{R}}$ and $\log L_{\text{X}}$. We varied A_i and B_i between 1.0–50.0 and 0.1–5.0, respectively, in increments of 0.1. In each case, we calculated the chi-squared: $[(\log L_{\text{Ri}} - \log L_{\text{R}})^2 + (\log L_{\text{Xi}} - \log L_{\text{X}})^2] / \epsilon_i^2$ where ϵ_i^2 is the combined error taking into account asymmetric errors, e.g. using $L_{\text{R-}}$ where $L_{\text{R}} > L_{\text{Ri}}$ and so on. We attempted to find values of A and B corresponding to optimum values of the reduced chi-squared, χ_i^2 , for the whole data set and for various subsamples (e.g. sorted by radio or X-ray class).

We obtained values of $\chi_i^2 > 5$ (very low significance) for most data selections including all those based on radio-selected AGN. The 10 radio-selected starbursts hosting X-ray-selected type-II AGN gave the most significant result, with $\chi_i^2 \sim 3$

$$\log L_{\text{X}} = (0.6 \pm 0.1)L_{\text{R}} + (21.4 \mp 2.4) \quad (16)$$

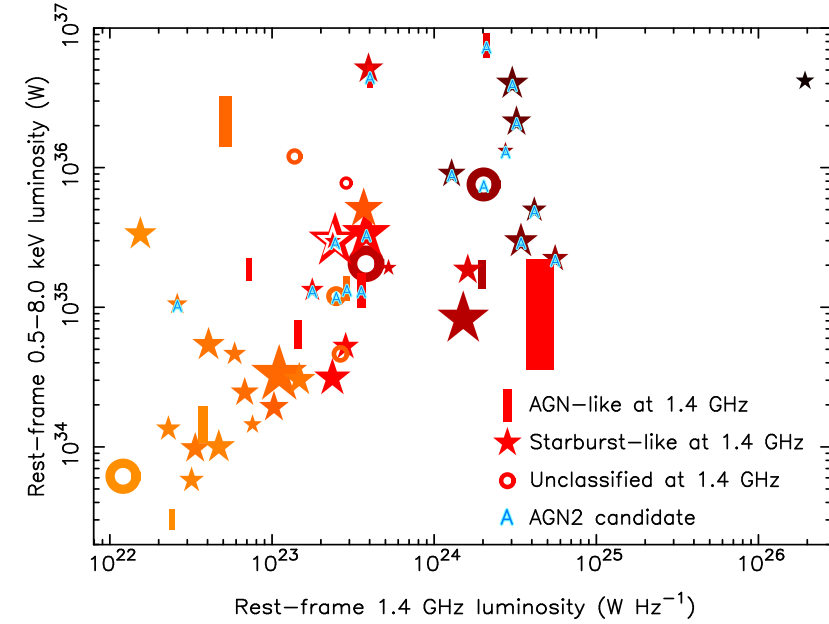


Fig. 4. The distribution of the classes of radio-bright sources (see key) with respect to L_R and L_X . The shade of red is proportional to redshift. The paler, brighter and darker symbols represent the approximate redshift ranges ($z < 1$), ($1 < z < 2$) and ($z > 2$), respectively. The size of the symbols is proportional to the source largest angular size. The blue ‘A’s represent X-ray selected type-II AGN; the highest redshift source may also be in this category. Three sources marked as starbursts also contain radio AGN (not shown to avoid overcomplicating this plot), see Fig. 6. Sources not detected at 1.4 GHz are not shown as they have no radio angular size measurements.

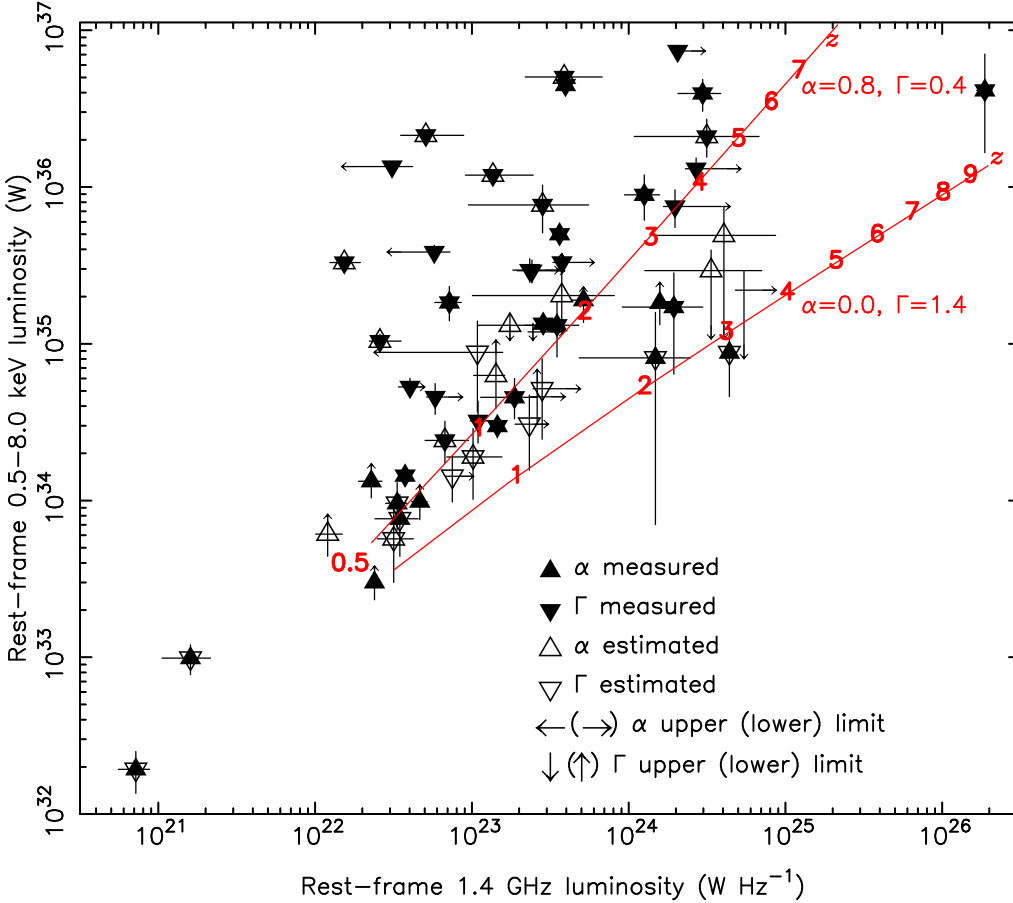


Fig. 5. The accuracy of L_R and L_X measurements. Uncertainties due to the spectral or photon index measurements are distinguished as shown in the key. See text for further explanations. The red lines show the detection limits at various redshifts for sources with the given combinations of α and Γ . For example, a source with $L_R = 10^{24} \text{ W m}^{-2}$ is detectable at $z < 2$ if it has $\alpha \sim 0$, but would be seen out to $z \sim 2.5$ if it had a steep radio spectrum. Its X-ray counterpart would be detected at $z \sim 2$ if it had $L_X > 5 \times 10^{34}$ and $\Gamma > 1.4$, but would need to have $L_X > 10^{35}$ if it had $\Gamma < 0.4$.

(the uncertainties show the range in which the minimum χ^2 was obtained), shown by the purple line in Figure 6. Including J123642+621331 as a radio starburst plus AGN (Section 5.3) gives an almost identical relationship, consistent with the suggestion that it may also host a type-II AGN, see Section 5.2. In any case, Tables 1 and 2 show that the lower error bound to Γ gives J123642+621331 a flat enough photon index to be a type-

II AGN and the corresponding value of L_X still fits within the uncertainties of Equation 16.

We obtained $3 < \chi_i^2 < 5$ for low-luminosity, low-redshift starbursts, e.g. $z < 1.3$, $L_X < 10^{35} \text{ W}$ (17 sources) gives

$$\log L_X = (0.95 \pm 0.05) \log L_R + 12.6 \pm 1.2 \quad (17)$$

shown by the green line in Figure 6. These coefficients are similar to those of Equation 1 (Bauer et al. 2002b), shown by the

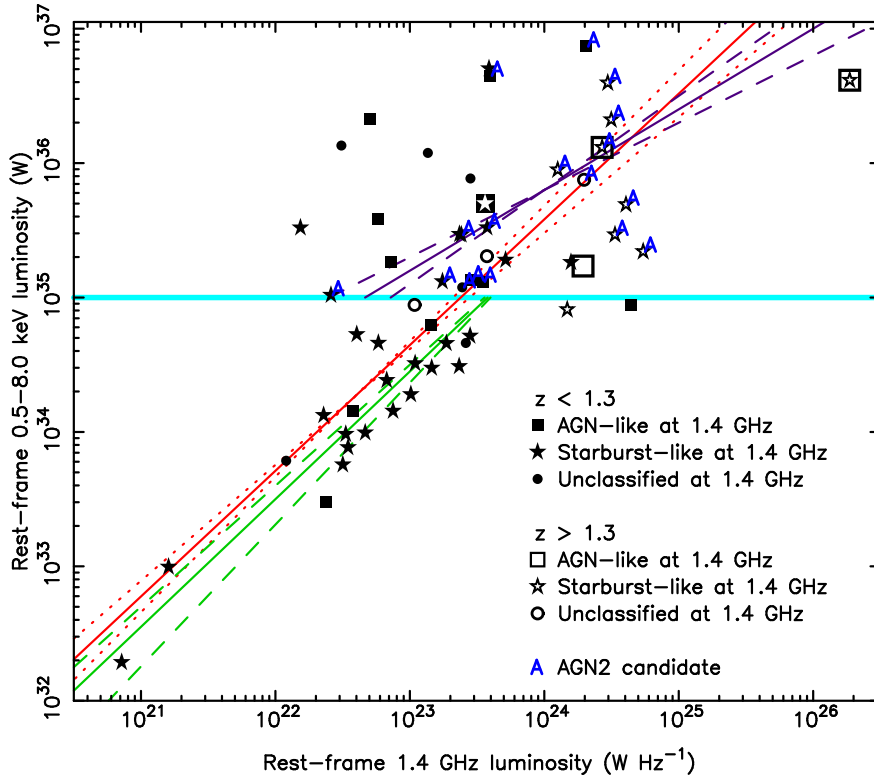


Fig. 6. X-ray luminosity as a function of radio luminosity for all 57 radio sources with X-ray counterparts and measured redshifts, classified as shown in the key (the squares enclosing stars are the three starbursts with apparent radio AGN cores; the lowest luminosity one is at $z < 1.3$). The X-ray luminosity limit for AGN, $L_X \approx 10^{35}$ W, is marked by a horizontal blue dividing line. The long red line is the relationship found by Bauer et al. (2002b) (Equation 1). The short green line shows the relationships for radio starbursts at $z < 1.3$ with $L_X < 10^{35}$ W (Equation 17). The short purple line shows the relationship for radio starbursts hosting X-ray selected type-II AGN (Equation 16) at $L_X > 10^{35}$ W. The dashed lines show the uncertainties for each relationship. The blue As indicate X-ray selected type-II AGN; the most radio-luminous sources may also be in this category.

red line in Fig. 6. The slight systematic offset to lower X-ray luminosities in our sample is probably because we used the 2 Ms data and a default of $\Gamma = 1.4$ where it was not measured. The low-redshift-dominated sample of Bauer et al. (2002b) has a higher average measured photon index and they took $\Gamma = 2$ for sources which did not have a measured value in the 1 Ms data. Six objects are common to both samples.

Barger et al. (2007) dispute the existence of the radio-X-ray luminosity relationship, as applied to high-redshift samples including the HDF(N), suggesting that it is a selection effect. We cannot compare this directly with our weak correlation given in Equations 16 and 17 since about half of our radio starbursts with obscured X-ray AGN and a third of low-X-ray luminosity starbursts have S_R less than their cutoff of $60 \mu\text{Jy}$, and our criteria for starburst classification is more specific to the origins of the radio emission than is their optical method. The significant point for both this paper and Barger et al. (2007) is that although a high proportion of high-redshift star-forming sources detected in the radio are also detected in X-rays, their luminosities are weakly correlated or uncorrelated, suggesting that the X-ray emission is of non-starburst origin.

Figure 6 also shows that 2 out of 4 radio AGN with $L_X < 10^{35}$ W lie close to the starburst-based relationships and the other 2 are under-luminous in X-rays (although one of these, the source with the lowest value of L_X/L_R , is the FR 1 J123644+621133, the only radio-X-ray crossmatched source to have jet-dominated radio emission). Conversely, only one each of a radio starburst and an unclassified source are present with $z > 1.3$ and $L_X < 10^{35}$ W although as shown by Fig. 5, such a source detected in one regime would also be detected in the other out to $z \sim 2$ for a typical starburst spectral index.

We emphasise that the significance of quantitative luminosity relationships is low for samples drawn exclusively from the HDF(N) data. The presence of X-ray and radio emission appears to be correlated (Section 2.5), but not the precise lumi-

nosities, whether starbursts or any other classes of objects are studied. The clear correlation between L_X and L_R found for samples dominated by lower-redshift sources does not apply to the high-redshift, high-luminosity sources. We already noted (in Section 2.5) that the nature of the overlap between radio and X-ray detections changes around $z \sim 1.1$, which supports our contention that the relationship between radio- and X-ray-emission mechanisms changes dramatically around $z = 1.1 - 1.3$.

6.2. Hard-band X-ray luminosity

The values of L_X given in Table 2, derived using Equation 11 in Section 4.2, do not take into account corrections for absorption nor for the intrinsic photon index. Padovani et al. (2004) derived the rest-frame X-ray luminosities for candidate type-2 AGN using the observed hard-band flux densities and assuming an intrinsic $\Gamma = 1.8$. We follow this method to calculate L_{XH} for all the cross-matched sources with published redshifts, shown as the arrow ends in Fig. 7. We looked for relationships between L_{XH} and L_R using a method similar to that described in Section 6.1 but obtained results of even lower significance.

Figure 7 shows that all the type-2 AGN have $L_{XH} > L_X$, as expected, and that the difference is greater for the more radio-luminous sources. All sources with arrow tips above the blue horizontal line have $L_{XH} > 10^{35}$ W, indicating the presence of an X-ray AGN (Alexander et al. 2003a; Cowie et al. 2004a).

We used Equation 1 to predict the full-band X-ray luminosity of starburst origin, L_{XSB} , assuming that L_R was entirely due to starburst activity. L_{XSB} is an overestimate where a significant fraction of radio emission is of AGN origin, although J123642+621331 is the only powerful starburst where over half the radio emission is AGN-powered (Section 5.1). As it has been shown empirically (e.g. Ranalli et al. 2003) that hard- and soft-band X-ray emission of starburst origin have similar dependencies in the relationships with emission of common origin in other

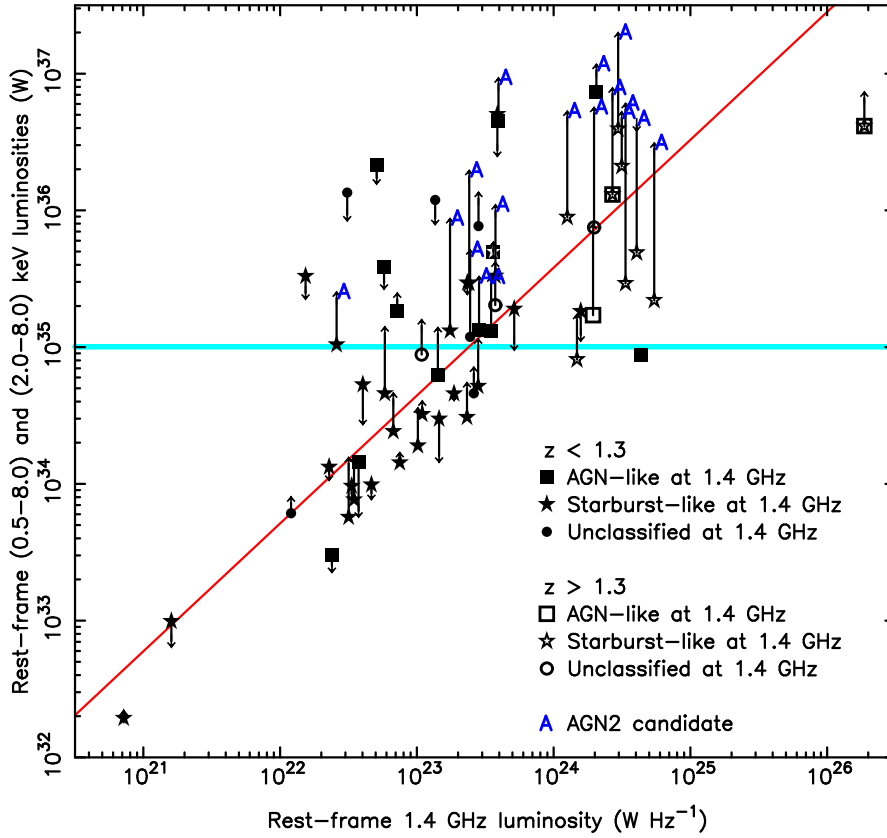


Fig. 7. The symbols, dividing line at $L_X \approx 10^{35}$ W and red line are as in Fig. 6. The arrow tips show the X-ray luminosity recalculated for the 2–8 keV rest-frame, L_{XH} , derived from the hard band flux densities using a constant $\Gamma = 1.8$ in Equation 11. The X-ray selected type-2 AGN are labelled at the L_{XH} values only.

regimes, the difference between the measured hard-band luminosity and L_{XSB} can thus be regarded as a lower limit to the X-ray luminosity of non-starburst origin. We find that $(L_{XH} - L_{XSB})$ exceeds 10^{35} W for all 17 type-2 AGN identified by Padovani et al. (2004), including the 10 radio starbursts, with a mean difference of $\geq 3.9 \times 10^{36}$ W (much greater than the total uncertainties) for either sub-sample. We interpret this as confirming that these galaxies must contain AGN, since the excess X-ray power, $\gg 10^{35}$ W, is very unlikely to be explained by any other mechanism. These values also suggest that, on average, $\leq 1/3$ of X-ray emission from obscured type-2 AGN is of starburst origin. All the radio starbursts with type-2 AGN remain sufficiently X-ray-bright to meet the AGN selection criteria, even using the lower luminosity limit derived here.

$L_{XH} - L_{XSB}$ is lower, at $\approx 1.6 \times 10^{36}$ W and $\approx 2.8 \times 10^{34}$ W for all radio-selected AGN and all starbursts respectively. Starbursts without type-II AGN show a very large scatter in the difference, about a mean of $\approx -2.1 \times 10^{36}$ W, showing that any AGN contribution is negligible in the majority of ‘pure’ starbursts.

7. X-ray-selected type-II AGN associated with radio-selected starbursts

7.1. A distinct population

Radio starbursts hosting type-2 AGN dominate the radio detections at high redshift, illustrated in Fig. 2. The 10-arcmin field contains 64 X-ray selected type-II AGN (as defined in Section 5.2), plus the candidate type-II AGN J123642+621331 (Sections 5.3 and 6.1). Eighteen of these have radio-bright counterparts (none are among the additional 7 8.4-GHz selected sources). 18/64 is a similar proportion to the quarter of all X-ray sources in the 10-arcmin field which are type-II AGN candi-

dates. Nine out of the 11 radio-bright X-ray sources at $z > 1.3$ host type-II AGN and this includes 8 out of the 9 radio starbursts in this redshift range.

Figure 4 and Table 1 show that the majority of the X-ray selected type-II AGN with radio counterparts are associated with starbursts (classified using the criteria in Section 5.1). The breakdown by radio source type, redshift and luminosity is shown in more detail in Figs. 8 and 9. The 3 radio starbursts (J123635+621424, J123642+621331 and J123642+621545) which also show signs of containing radio AGN (Section 5.1) are only shown once, as starbursts. J123635+621424, and probably J123642+621331, are also X-ray selected type-II AGN.

Radio AGN outnumber starbursts 2:1 in the most powerful third ($S_R > 100 \mu\text{Jy}$) of all 92 radio-bright sources whilst starbursts are an even greater majority among the fainter sources. The radio-selected AGN are on average intrinsically more radio-luminous than the starbursts. The median redshift of all radio AGN is higher compared with all starbursts in the HDF(N) and they appear to be separate populations (Muxlow et al. 2005). The high redshift radio-selected starbursts associated with obscured X-ray selected AGN appear to be a third class, distinct from the radio-bright AGN and from the majority of the starbursts.

Figure ?? shows a remarkable segregation between high- Γ , low- z , sources of all classes but without type-II AGN, and low- Γ sources. Of the latter, the radio starbursts and unclassified sources with type-II AGN (including the candidate J123642+621331) show a slight correlation between Γ and z , consistent with the change in X-ray spectral slope expected for highly obscured sources at higher rest-frame energies (Section 5.2). The blue $\Gamma(z)$ line is a very rough estimate of the change in the observed Γ with increasing redshift, for a rest-frame $\Gamma = 0$, based on the spectral models shown in Alexander et al. (2005a), their fig. 7, for sources with $N_H \gtrsim 2 \times 10^{27} \text{ m}^{-2}$.

All but 3 out of 16 sources with a Γ below the estimated $\Gamma(z)$ line contain type-II AGN and the majority are radio starbursts; the only radio-bright AGN here is not a type-II AGN.

The 4 radio-bright AGN with X-ray type-II AGN all lie above this line, suggesting that they do not reach the highest degrees of obscuration. The segregation is not due to Compton-thick absorption as signs of this are only seen in one source, J123622+621629, a radio starburst hosting a type-II AGN, (Alexander et al. 2003b).

Although all but 2 of the radio AGN with measured redshifts are detected by *Chandra*, the non-detections are the highest-redshift sources; in contrast, all the starbursts known to have $z > 1.3$ have X-ray counterparts. Figures 8 and 9 (panels a and b) show that the distributions of X-ray selected type-II AGN are biased towards much higher redshifts and luminosities than the distributions of radio-classified AGN or unclassified radio sources. The population of type-II AGN does overlap closely the high redshift/high luminosity end of the distribution of radio-selected starbursts (panel c).

7.2. Radio-bright SMG starbursts with type-II AGN

There are strong similarities between the redshift distributions of the radio SMGs and type-II AGN (Figs. 8 and 9, panel d), especially at higher z . 20% of all radio-bright galaxies detected by *Chandra* are also SCUBA sources (Section 2.4.2) and nearly half of these contain type-II AGN. We noted a low correlation between L_X and L_R for high-redshift starbursts (Section 6.1); a similar large scatter was seen by Borys et al. (2004) for a SCUBA-selected subsample of 10 sources.

Alexander et al. (2005a) calculated the radio and X-ray luminosities for all SMG with spectroscopic redshifts, in the overlap between the *Chandra* and VLA fields of view. All except one have X-ray luminosities in excess of the relationship predicted from star formation, by over an order of magnitude in the case of the type-II AGN candidates (as we also found in Section 6.2). The X-ray selected type-II AGN also have an FIR/X-ray luminosity ratio about an order of magnitude greater than the typical ratio for nearby QSO, showing that at least 90% of the FIR emission is probably of starburst origin, at an SFR of order $1000 M_\odot \text{ yr}^{-1}$.

7.3. Extended radio emission, compact X-ray cores

The starburst interpretation of sub-mm emission from SMG which are hard X-ray sources is only questionable if they possess nuclear dust to much greater optical depths than is seen around local AGN (Section 1; Alexander et al. 2005a). We summarise the evidence that these objects do contain extended starbursts which are distinct from any AGN cores.

The radio starburst classification is based on distinctive morphology and spectral index (Section 5.1; Muxlow et al. 2005). The median angular size of radio-bright AGN with X-ray counterparts is $\sim 0''.6$ whilst for starbursts it is $\sim 1''.4$ (Table 1; Fig. 4). SCUBA galaxies which are most extended in the radio are also more likely to be X-ray bright; of the 12 SMG radio sources studied by Chapman et al. (2004b), the 6 with the largest 1.4-GHz angular sizes all had X-ray counterparts but only 2 of the 4 smallest radio sources had X-ray counterparts.

X-ray emission from many of the the starburst galaxies would, however, be resolved, if it had a common origin with the radio emission, which is not seen – all 55 X-ray sources are smaller than the $1''$ *Chandra* FWHM in this region.

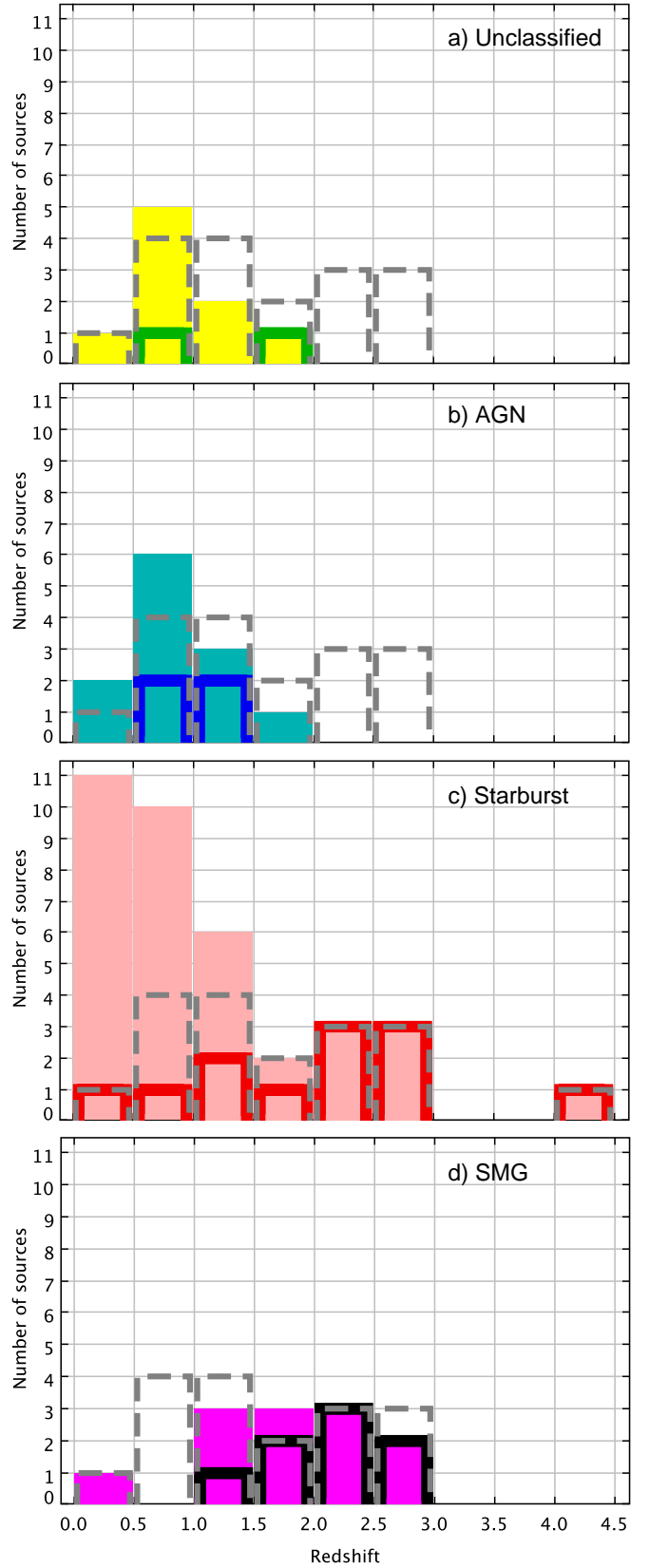


Fig. 8. Redshift distribution of radio/X-ray sources according to radio classification and counterparts. In each panel the dashed grey line shows the distribution of sources which have X-ray type-II AGN signatures (including J123642+121331, Section 5.3) and the solid line shows their counterparts in the sub-sample. The filled area shows the total number of sources with radio properties which are a) unclassified, b) AGN-like or c) starburst-like; panel d) shows radio sources with SCUBA counterparts.

Nine out of the 10 radio-bright X-ray sources which are also SMG are radio starbursts with $\alpha \geq 0.7$ (including 7 with type-II AGN) and the tenth is unclassified. The mean radio angular size is $1''.3$ and only J123635+621424, a starburst with a radio AGN core, is smaller than $0''.6$. Chapman et al. (2004b) found a similar result, obtaining a typical extent of $1''$ for the radio counterparts to a sample of dozen SMGs. Pope et al. (2005) found that the optical ACS counterparts of SMG at $z < 2$ in the HDF(N) have radii in the range $\sim 1'' - \sim 2''.5$, which is significantly larger than field galaxies at the same redshift. Similarly, more distant ($z \approx 2.5$), highly reddened galaxies with SEDs consistent with vigorous star formation are typically over twice the size of non-starformers in *HST NICMOS* images of the HDF(S) (Zirm et al. 2006).

We conclude that, although present instruments cannot resolve MIR or sub-mm sources on the scale of radio or optical emission with starburst characteristics, the close association supports a common origin. In contrast, X-ray emission from the same sources is consistently more compact than the radio emission and appears to have a distinctly different origin.

8. The nature of very faint radio and X-ray sources

At high redshifts, the present generation of radio and X-ray surveys are biased towards extreme objects, as whatever was ‘normal’ at $z \gg 1$ is below the threshold for secure detections of individual sources. In advance of *e*-MERLIN, the EVLA and XEUS, stacking is the only method to investigate the radio and X-ray properties of objects at $z > 1$ with $L_R < 10^{23}$ W Hz $^{-1}$ or $L_X < 10^{34}$ W. Muxlow et al. (2005) demonstrated the existence of such a radio population by finding a statistical excess of $1-6\sigma$ radio flux on arcsec scales at the positions of *ISO* sources and of optical (*HST WFPC2*) galaxies with $I \lesssim 24$ mag in the 3-arcmin field. The MERLIN+VLA images are more than twice as sensitive as the VLA-only data but no new sources were detected in the 3-arcmin field between $27-40 \mu\text{Jy}$, suggesting that any objects just below the VLA completeness limit are extended over $\gtrsim 2''$ with no hotspots. Garrett et al. (2000) showed that about 10% of radio sources in the HDF(N) are probably resolved out even at $2''$ resolution so even stacking MERLIN+VLA data will not recover these.

We analyse the excess radio flux at the positions of *Chandra* sources in the recently-made 8-arcmin radio image convolved with a restoring beam of $0''.4$ (see Section 3.2). Muxlow et al. (2006) and Beswick et al. (2006) present similar analyses at the positions of ACS and *Spitzer* sources.

8.1. Radio-faint Chandra sources

181 X-ray sources from the catalogue of Alexander et al. (2003b) lie within the 8-arcmin MERLIN+VLA 1.4-GHz image. We used the matching criteria described in Section 2.2 to divide the X-ray sources into 39 sources with radio counterparts brighter than $40 \mu\text{Jy}$ (“radio-bright”), and 142 without (“radio-faint”). For each sample, we stacked the 1.4-GHz radio flux density enclosed by $0''.25$ to $2''$ radius circles centred on the X-ray source positions. We constructed control samples by stacking the radio flux at positions offset by $10''$ from each X-ray source (checking that these did not coincide with known X-ray or radio sources or their sidelobes). The noise distribution is slightly non-Gaussian due to confusing sources in the sidelobes of the heterogeneous primary beams but there are no artifacts $> 7\sigma$ ($\approx 27 \mu\text{Jy}$ per $0''.2 - 0''.5$ beam) apart from sidelobes very close to the 3 sources brighter than 1 mJy, J123644+621133, J123714+620823 and

J123725+621128 (Muxlow et al. 2005). The average stacked flux density from the radio-faint sources increased up for radii up to $\sim 1''$ and levelled off for higher radii, so we report results for $1''$ radii. The variance in each bin is $3-4 \mu\text{Jy}$ (the radio map 1σ level) and the control samples for the radio-faint sources are all $< 3\sigma$.

The stacking intervals were sorted by X-ray flux density, photon index and redshift, into bins containing almost equal numbers of measurements. In each of Figs ?? and ?? the scale on the abscissa shows the median value in each bin.

8.1.1. Stacking by X-ray flux density

We present results for stacking sorted by full, soft, hard and very hard (4–8 keV) band flux density. We plot the relationship between the mean stacked radio flux density and the X-ray flux density in each of 5 bins with 28 or 29 (7 or 8) samples in each bin for the radio-faint (-bright) sources. We treated upper limits as values; hence the nominal value for the bottom bin may be greater than the true median X-ray flux but it does not affect the significance of the results. The filled symbols in Fig. ??, upper panel, show the stacked radio flux at the X-ray positions of radio-faint sources (see key) and the hollow symbols show the corresponding control values. This shows that the mean stacked radio flux density is significantly above the control for all bins apart from the faintest very hard band bin. The average radio flux density is similar for any soft-band X-ray flux density, but becomes increasingly correlated with X-ray flux density for the hard and very hard bands. Figure ??, lower panel, shows that there is no correlation with any band for radio-bright sources (the four high values are biased by one very bright radio source), as discussed in Section 6.

8.1.2. Stacking by photon index

84 (29) radio-faint (-bright) X-ray sources have at least partly measured photon indices (Γ) (i.e. detected in at least one sub-band as well as full band). We plot the mean stacked radio flux density against the X-ray photon index in each of 4 bins evenly spaced in Γ , which gives similar source counts in each bin. Figure ?? shows that radio-faint X-ray sources (heavy circles) with $\Gamma < 0.6$ have a mean radio flux density twice that for sources with $\Gamma > 1.4$. This is not the case for the radio-bright sources (heavy triangles).

8.1.3. Stacking by redshift

76 (35) radio-faint (-bright) X-ray sources have measured redshifts. In each case we divided them into 4 bins with approximately equal numbers of samples in each bin. There is no obvious correlation for either sample.

8.2. The nature of radio-faint X-ray sources

There is a significant excess of radio flux at the positions of *Chandra* sources without formally identified radio counterparts. These have typical 1.4-GHz flux densities from $\approx 20 - 40 \mu\text{Jy}$ per $1''$ -radius circle ($\equiv 6 - 13 \mu\text{Jy arcsec}^{-2}$). This is the median largest angular size of radio sources above $40 \mu\text{Jy}$ (Muxlow et al. 2005) and is three times the median *Chandra* position error for the sources within the 8-arcmin field (Section 2.2).

The most obvious correlations for radio-quiet sources are the association of a higher average radio flux density with a higher

X-ray flux density in the full or harder bands, and with a lower Γ . The average radio flux density approaches $40 \mu\text{Jy}$ for radio-quiet X-ray sources with flux densities $> 10^{-18} \text{ W m}^{-2} \text{ Hz}^{-1}$ or with hard photon indices, suggesting that the majority of these (probably obscured) X-ray sources have genuine radio counterparts. We examined the radio-quiet images at the position of each *Chandra* source by plotting contours at 3, 4, 5 and $6 \sigma^{13}$. Eleven sources are $> 20 \mu\text{Jy}$ (5σ). Their apparently extended radio flux and the absence of hotspots brighter than $27 \mu\text{Jy}$ per $0''.4$ beam, corresponding to maximum brightness temperatures of less than a few 100 K, suggests that these sources are part of the radio starburst population and do not contain radio-bright AGN. Seven of the corresponding X-ray objects have a measured photon index of which 5 have $\Gamma < 1$ and 4 are listed as type-II AGN by Padovani et al. (2004). A similar proportion (40%) of all 142 radio-faint *Chandra* sources have low, measured photon indices characteristic of obscured AGN.

The stacked-average photon index for the whole *Chandra* HDF(N) field becomes flatter for lower X-ray count rates and then slightly steepens again (Alexander et al. 2003b). The composite X-ray spectra of the most obscured *Chandra* sources ($N_{\text{H}} > 5 \times 10^{27} \text{ m}^{-2}$) show an upturn at rest frame energies $< 4 \text{ keV}$, attributed to star formation (Alexander et al. 2005a). This is independent evidence for the association between obscured AGN and starburst activity.

X-ray sources associated with individual galaxies in the 8-arcmin field are smaller than the $\approx 1''$ resolution of *Chandra*, and none are among the extended emission sources identified by Bauer et al. (2002a). About 20% (29/142) of the radio-faint X-ray sources have $F_{\text{X}} > 0.3 \times 10^{-18}$ and $\Gamma > 1.4$. Equation 1 predicts a radio flux density $> 40 \mu\text{Jy}$ from such sources if the X-ray emission is of starburst origin, so they would have been detected as radio-bright if the radio and X-ray emission had a common starburst origin. Instead, it is likely that these radio-quiet sources contain unobscured X-ray AGN.

Almost all the remaining 40% of the radio-faint sources, with $F_{\text{X}} \leq 0.3 \times 10^{-18}$, do not have measured photon indices (Bauer et al. 2004). Reddy & Steidel (2004) stacked *Chandra* soft-band and VLA-only radio HDF(N) flux densities for (rest-frame) UV-selected objects at a mean redshift of ~ 2 . Their measurements were consistent with the relationship found by Bauer et al. (2002b), giving an average SFR of $\sim 50 \text{ M}_{\odot} \text{ yr}^{-1}$. Stacking *Chandra* data for Lyman Break galaxies out to $z = 6$, gave similar results. Their selection criteria (optical detection, soft-band dominated) excluded objects like the SMGs and the most vigorous radio starbursts associated with type-II AGN, so these sources are probably analogues of the local ULIRGs.

In Section 2.5 we used the Kolmogorov-Smirnov test to show that there seemed to be a change in the relationship between radio and X-ray sources at redshifts above and below ~ 1.1 . We also found (Section 6.1) a starburst-like relationship between L_{R} and L_{X} for most low-redshift sources, but only very weak relationships at high redshift, most significant for the radio starbursts hosting type-II AGN. The correlation between radio-faint radio flux density and harder X-ray emission seen in Fig. ?? (upper) is consistent with a continuation of this relationship for the radio-faint sources. The correlation with harder photon index is also consistent with type-II AGN powering the dominant population of distant X-ray sources with radio counterparts of a few tens of μJy .

In summary, we predict that future instruments will confirm that the association between the presence of X-ray and radio

emission extends to radio flux densities $\lesssim 10 \mu\text{Jy arcsec}^{-2}$. The available evidence suggests that two fifths of these sources will be found to be radio starbursts hosting obscured X-ray AGN, probably at high redshifts, one fifth are radio-quiet, unobscured AGN and the remainder are probably ULIRGs.

9. Conclusions

We have used Virtual Observatory tools and RadioNet software to compare the radio and X-ray properties of galaxies at $z \lesssim 4.5$ in the HDF(N). 92 radio-bright objects ($S_{\text{R}} > 40 \mu\text{Jy}$) are resolved by MERLIN+VLA at 1.4 GHz. 55 of these sources are also securely detected by *Chandra* and the majority of these sources have spectral/photon indices based on measurements at more than one frequency. Where spectral/photon indices are estimated, we have not used the values as primary diagnostics.

9.1. The majority of radio starbursts in the HDF(N) have X-ray counterparts

The combination of radio morphologies and spectral indices, in some cases supported by rest-frame MIR measurements, provides reliable diagnostics for the origins of the radio emission from most of the sources (Section 5; Muxlow et al. 2005). 70% of radio starbursts have X-ray counterparts. Radio starbursts outnumber radio AGN by 3:1 for classified sources in the whole radio-bright sample and the same proportion is seen for the 55 sources with X-ray counterparts. Seven unresolved 8.4-GHz sources which are not radio-bright at 1.4 GHz also have X-ray counterparts are not included in most of this analysis, but they appear to contain a similar majority of starbursts. In contrast, the X-ray emission is of AGN origin in about 80% of all *Chandra* sources (Bauer et al. 2002b).

Optical spectroscopy finds approximately equal numbers of star formers and AGN (Cowie et al. 2004a) and only 6 optically-classified starbursts in the HDF(N) have X-ray counterparts (along with 29 optical AGN). Similarly, only a few percent of the starbursts found using *BzK* criteria, (Daddi et al. 2004), have soft-X-ray counterparts (Daddi et al. 2005) (hard-X-ray sources were excluded from their sample). These results imply that many radio starbursts which are too obscured to be identified using optical or even NIR spectroscopy and photometry, are a separate population with a much higher proportion of X-ray counterparts.

9.2. High-luminosity radio and X-ray emission has separate origins with the same galaxies

There is no discernible relationship between either the radio and X-ray flux densities or the *K*-corrected luminosities for the cross-matched sample as a whole. The close relationship between L_{R} and L_{X} established by Bauer et al. (2002b) breaks down at $z \gtrsim 1.3$, even if only radio starbursts are considered (Section 6.1). The X-ray emission predicted from the radio luminosity of these sources is on average less than 1/3 of the observed X-ray luminosity and even after subtracting the potential starburst contribution, the hard-band X-ray luminosity of the type-II AGN still exceeds 10^{35} W (Section 6.2). At least half of the radio sources with X-ray counterparts have a largest angular size greater than the *Chandra* resolution of $\approx 1''$ but all the X-ray sources are unresolved.

The presence of detectable radio emission is significantly correlated with the probability of also detecting X-rays, and vice versa (Bauer et al. 2002b) but our results strongly suggest that

¹³ An image cut-out service will be available via AstroGrid.

the radio and X-ray emission originates from separate phenomena in most sources at $z \gtrsim 1.1$.

9.3. A distinct population of high-redshift radio/sub-mm starbursts associated with X-ray-selected obscured AGN

The fraction of X-ray sources with radio counterparts increases significantly at $z \gtrsim 1.1$ (Fig. 2). Section 7 sums up the evidence that high- z radio- or sub-mm-selected starbursts are a separate population from starforming galaxies at $z \lesssim 1.3$ and indeed exceed the activity seen in local ULIRGs (e.g. Section 2.4.2 and references therein.)

A hard photon index $\Gamma \leq 1$ (at rest-frame 0.5–8 keV) combined with $L_X > 10^{35}$ W shows the presence of an obscured type-II AGN and 18 such objects identified by Padovani et al. (2004) have radio counterparts in the HDF(N). Model X-ray spectra extending to high rest-frame energies (Alexander et al. 2005a) suggest that type-II AGN at $z \gtrsim 2$ could have slightly higher Γ as measured by *Chandra*. This is supported by the L_R – L_X relationship and Γ – z distribution of type-II AGN with radio counterparts (Fig. ??) which leads us to propose that J123642+621331, at $z = 4.424$ with observed $\Gamma = 1.35^{+0.34}_{-0.40}$, also contains a type-II AGN. Twelve of the type-II AGN (including this source) have radio starburst hosts.

The great majority (22/27) of 15 or 16 μm detections among the radio+X-ray sources are not type-II AGN hosts. They have a mean redshift of 1 and a mean photon index of 1.6. They appear more analogous to local ULIRGs than to the more extreme SMGs. Well-studied ULIRGs such as Arp 220 or Markarian 231 possess nuclear starbursts which would be barely resolved at the maximum detectable $z \sim 1$. Bauer et al. (2004) noted that the relative number counts of starburst and AGN X-ray sources changed from a large AGN majority over most of the flux density range sampled by *Chandra* to a higher proportion of starbursts among the faintest sources, likely to correspond to the less active tail of a relatively nearby population. The faintest $\sim 40\%$ of X-ray sources which are radio-quiet, but have a significant radio flux density revealed by stacking, (Section 8.2), may also be ULIRGs.

In contrast, the SMG counterparts have a mean redshift of 1.8 and an average photon index of 0.6, suggesting that type-II AGN contribute substantially more of the X-ray emission. Alexander et al. (2005b) suggest that between a third and a half of the entire SCUBA source population contain AGN. 2/3 of radio-bright sources with X-ray and SCUBA emission contain type-II AGN. About 40% of the radio-faint sources found by stacking are associated with hard X-ray sources are probably also radio starbursts hosting obscured AGN. The radio starbursts appear to be extended over 2 – 10 kpc or more, an order of magnitude larger than those in the local universe. The SMG (at a median redshift of at least 2.2) have star formation rates of the order of $1000 M_\odot \text{ yr}^{-1}$, also about 10 times higher than that of local ULIRGs.

9.4. Implications for galaxy evolution

Both starburst activity and feeding a black hole probably result from major mergers, which are increasingly common at $z > 1.5$ and dominate galaxy growth at $z > 2$ (Conselice et al. 2005). The comoving luminosity densities for AGN and for starbursts increases as $(1+z)^{2.3}$ for $z \lesssim 1.5$, using optical, IR, X-ray and radio classifications and luminosities (Barger et al. 2005; Cowie et al. 2004a). Current estimates of the star formation rate as a

function of redshift (Hopkins & Beacom 2006) suggest that the star formation rate continues to increase out to redshifts of 3 or more. It is possible that sub-mm galaxies at unknown redshifts may be even more vigorous starbursts at $z \gtrsim 3$ (Ivison et al. 2007).

The one radio-bright object in the HDF(N) with a known redshift greater than 3, J123642+621331 at $z = 4.424$, appears to contain both a (probably obscured) AGN and a very productive starburst. Stacking 1.4-GHz emission from radio-faint sources at the position of objects detected by *Chandra* shows a statistically significant excess which rises with decreasing Γ and with increasing hard-band X-ray flux densities (Section 8.2). Eleven individual radio-faint counterparts to X-ray sources are $> 5\sigma$ ($> 20 \mu\text{Jy}$), all of which appear extended and lacking radio hotspots, consistent with these sources being a faint or high-redshift tail of the radio starbursts associated with type-II AGN.

Within the next 2 years, *e-MERLIN*+*EVLA* images should reveal many more high-redshift μJy galaxies with optical, *Spitzer* or *SCUBA*(2) counterparts, pushing measurements of the star formation rate (and redshifts) back to $z \gtrsim 5$, whilst the ongoing increase in capacity of the VLBI correlator at JIVE will enable distant compact radio AGN cores to be distinguished from even sub-kpc-scale starbursts (Garrett et al. 2005).

Acknowledgements. This work is based in part on observations made with the Multi Element Radio-Linked Interferometer Network (MERLIN), operated by Manchester University on behalf of PPARC, and with the Very Large Array, a facility of the NSF operated under cooperative agreement by Associated Universities, Inc. This work has benefited from research funding from the EC Framework 6 Programme under RadioNet R113CT 2003 5058187. We employed software provided by the UK AstroGrid Virtual Observatory Project, funded by PPARC and the Framework 6 Programme and we also used the Vizier catalogue access tool and the ADS bibliographic service.

We thank the MERLIN and VLA staff for considerable assistance with observations. AMSR acknowledges the hospitality provided by CDS, where she was a ‘professeur invité’ during part of this work. We thank P. Padovani (ESO) for helpful discussions and we are extremely grateful to the anonymous referee for improving the accuracy, clarity and consistency of the paper.

References

- Alexander, D. M., Aussel, H., Bauer, F. E., et al. 2002, *ApJ*, 568, L85
- Alexander, D. M., Bauer, F. E., Brandt, W. N., et al. 2003a, *AJ*, 125, 383
- Alexander, D. M., Bauer, F. E., Brandt, W. N., et al. 2003b, *AJ*, 126, 539
- Alexander, D. M., Bauer, F. E., Chapman, S. C., et al. 2005a, *ApJ*, 632, 736
- Alexander, D. M., Smail, I., Bauer, F. E., et al. 2005b, *Nature*, 434, 738
- Aussel, H., Cesarsky, C. J., Elbaz, D., & Starck, J. L. 1999, *A&A*, 342, 313
- Barger, A. J., Cowie, L. L., Brandt, W. N., et al. 2002, *AJ*, 124, 1839
- Barger, A. J., Cowie, L. L., Capak, P., et al. 2003, *AJ*, 126, 632
- Barger, A. J., Cowie, L. L., Mushotzky, R. F., et al. 2005, *AJ*, 129, 578
- Barger, A. J., Cowie, L. L., Trentham, N., et al. 1999, *AJ*, 117, 102
- Barger, A. J., Cowie, L. L., & Wang, W.-H. 2007, *ApJ*, 654, 764
- Barthel, P. D. & Miley, G. K. 1988, *Nature*, 333, 319
- Bauer, F. E., Alexander, D. M., Brandt, W. N., et al. 2002a, *AJ*, 123, 1163
- Bauer, F. E., Alexander, D. M., Brandt, W. N., et al. 2002b, *AJ*, 124, 2351
- Bauer, F. E., Alexander, D. M., Brandt, W. N., et al. 2004, *AJ*, 128, 2048
- Beswick, R. J., Muxlow, T. W. B., Thrall, H., & Richards, A. M. S. 2006, in *At the Edge of the Universe*, ed. J. Alfonso, H. Ferguson, & R. Norris, ASP Conference Series, astro-ph/0612077
- Blain, A. W., Smail, I., Ivison, R. J., Kneib, J.-P., & Frayer, D. T. 2002, *Phys. Rep.*, 369, 111
- Borys, C., Scott, D., Chapman, S., et al. 2004, *MNRAS*, 355, 485
- Chapman, S. C., Blain, A. W., Smail, I., & Ivison, R. J. 2005, *ApJ*, 622, 772
- Chapman, S. C., Smail, I., Blain, A. W., & Ivison, R. J. 2004a, *ApJ*, 614, 671
- Chapman, S. C., Smail, I., Windhorst, R., Muxlow, T., & Ivison, R. J. 2004b, *ApJ*, 611, 732
- Chi, S., Garrett, M. A., & Barthel, P. D. 2006, in 8th EVN Symposium, ed. A. Marecki, *Proceedings of Science (SISSA, Trieste)*, <http://os.sissa.it/archive/conferences/036/>
- Cohen, J. G. 2001, *AJ*, 121, 2895
- Cohen, J. G., Cowie, L. L., Hogg, D. W., et al. 1996, *ApJ*, 471, L5
- Cohen, J. G., Hogg, D. W., Blandford, R., et al. 2000, *ApJ*, 538, 29

Condon, J. J. 1992, *ARA&A*, 30, 575

Conselice, C. J., Bershad, M. A., Dickinson, M., & Papovich, C. 2003, *AJ*, 126, 1183

Conselice, C. J., Blackburne, J. A., & Papovich, C. 2005, *ApJ*, 620, 564

Cowie, L. L., Barger, A. J., Fomalont, E. B., & Capak, P. 2004a, *ApJ*, 603, L69

Cowie, L. L., Barger, A. J., Hu, E. M., Capak, P., & Songaila, A. 2004b, *AJ*, 127, 3137

Cram, L., Hopkins, A., Mobasher, B., & Rowan-Robinson, M. 1998, *ApJ*, 507, 155

Daddi, E., Cimatti, A., Renzini, A., et al. 2004, *ApJ*, 600, L127

Daddi, E., Dickinson, M., Chary, R., et al. 2005, *ApJ*, 631, L13

Dawson, S., Stern, D., Bunker, A. J., Spinrad, H., & Dey, A. 2001, *AJ*, 122, 598

Downes, D. & Solomon, P. M. 1998, *ApJ*, 507, 615

Elbaz, D., Cesarsky, C. J., Chantal, P., et al. 2002, *A&A*, 384, 848

Evans, D. A., Worrall, D. M., Hardcastle, M. J., Kraft, R. P., & Birkinshaw, M. 2006, *ApJ*, 642, 96

Fanaroff, B. L. & Riley, J. M. 1974, *MNRAS*, 167, 31P

Fomalont, E. B., Kellermann, K. I., & Partridge, R. B., e. a. 2002, *AJ*, 123, 2402

Frayer, D. T., Ivison, R. J., Scoville, N. Z., et al. 1998, *ApJ*, 506, L7

Garrett, M. A. 2002, *A&A*, 384, L19

Garrett, M. A., de Bruyn, A. G., Giroletti, M., Baan, W. A., & Schilizzi, R. T. 2000, *A&A*, 361, L41

Garrett, M. A., Muxlow, T. W. B., Garrington, S. T., et al. 2001, *A&A*, 366, L5

Garrett, M. A., Wrobel, J. M., & Morganti, R. 2005, in *ASP Conf. Ser. 340: Future Directions in High Resolution Astronomy*, ed. J. Romney & M. Reid, 600

George, I. M., Turner, T. J., Yaqoob, T., et al. 2000, *ApJ*, 531, 52

Giallisco, M., Ferguson, H. C., Koekemoer, A. M., et al. 2004, *ApJ*, 600, L93

Goldschmidt, P., Oliver, S. J., Serjeant, S. B. G., et al. 1997, *MNRAS*, 289, 465

Griffiths, R. E., Ptak, A., Feigelson, E. D., et al. 2000, *Science*, 290, 1325

Grimm, H.-J., Gilfanov, M., & Sunyaev, R. 2003, *MNRAS*, 339, 793

Hopkins, A. M. & Beacom, J. F. 2006, *ApJ*, 651, 142

Hornschemeier, A. E., Brandt, W. N., Garmire, G. P., et al. 2001, *ApJ*, 554, 742

Hughes, D. H., Serjeant, S., Dunlop, J., et al. 1998, *Nature*, 394, 241

Ivison, R. J., Chapman, S. C., Faber, S. M., et al. 2007, *ApJ*, 660, L77

Kettenis, M. M., van Langevelde, H. J., Reynolds, C., & Cotton, B. 2006, in *ASP Conf. Ser. 351: Astronomical Data Analysis Software and Systems XV*, ed. C. Gabriel, C. Arviset, D. Ponz, & S. Enrique, 497

Madau, P., Ferguson, H. C., Dickinson, M. E., et al. 1996, *MNRAS*, 283, 1388

Morrison, G., Dickinson, M., Owen, F., et al. 2006, in *ASP Conf. Ser. Infrared Diagnostics of Galaxy Evolution (Spitzer Conference)*, ed. R.-R. Chary, *astro-ph/0603412*

Muxlow, T. W. B., Beswick, R. J., Thrall, H., et al. 2006, in *At the Edge of the Universe*, ed. J. Alfonso, H. Ferguson, & R. Norris, *ASP Conference Series*

Muxlow, T. W. B., Richards, A. M. S., Garrington, S. T., et al. 2005, *MNRAS*, 358, 1159

Norman, C., Ptak, A., Hornschemeier, A., et al. 2004, *ApJ*, 607, 721

Padovani, P., Allen, M. G., Rosati, P., & Walton, N. A. 2004, *A&A*, 424, 545

Pope, A., Borys, C., Scott, D., et al. 2005, *MNRAS*, 358, 149

Ptak, A., Serlemitsos, P., Yaqoob, T., & Mushotzky, R. 1999, *ApJS*, 120, 179

Ranalli, P., Comastri, A., & Setti, G. 2003, *A&A*, 399, 39

Reddy, N. A. & Steidel, C. C. 2004, *ApJ*, 603, L13

Richards, E. A. 2000, *ApJ*, 533, 611

Richards, E. A., Kellermann, K. I., Fomalont, E. B., Windhorst, R. A., & Partridge, R. B. 1998, *AJ*, 116, 1039

Rosa-Gonzalez, D., Burgarella, D., Nandra, K., et al. 2007, *MNRAS*, *arXiv:0705.1278v1*

Sadler, E. M., Jackson, C. A., Cannon, R. D., et al. 2002, *MNRAS*, 329, 227

Serjeant, S., Dunlop, J. S., Mann, R. G., et al. 2003, *MNRAS*, 344, 887

Smail, I., Ivison, R. J., Blain, A. W., & Kneib, J.-P. 2002, *MNRAS*, 331, 495

Snellen, I. A. G. & Best, P. N. 2001, *MNRAS*, 328, 897

Soifer, B. T., Neugebauer, G., Matthews, K., et al. 2000, *AJ*, 119, 509

Szokoly, G. P., Bergeron, J., Hasinger, G., et al. 2004, *ApJS*, 155, 271

Teplitz, H. I., Charmandaris, V., Chary, R., et al. 2005, *ApJ*, 634, 128

Waddington, I., Windhorst, R. A., & Cohen, S. H., e. a. 1999, *ApJ*, L77

Wang, W.-H., Cowie, L. L., & Barger, A. J. 2004, *ApJ*, 613, 655

Williams, R. E., Blacker, B., Dickinson, M., et al. 1996, *AJ*, 112, 1335

Yun, M. S. & Carilli, C. L. 2002, *ApJ*, 568, 88

Yun, M. S., Reddy, N. A., & Condon, J. J. 2001, *ApJ*, 554, 803

Zirm, A. W., van der Wel, A., Franx, M., et al. 2006, *ApJ*

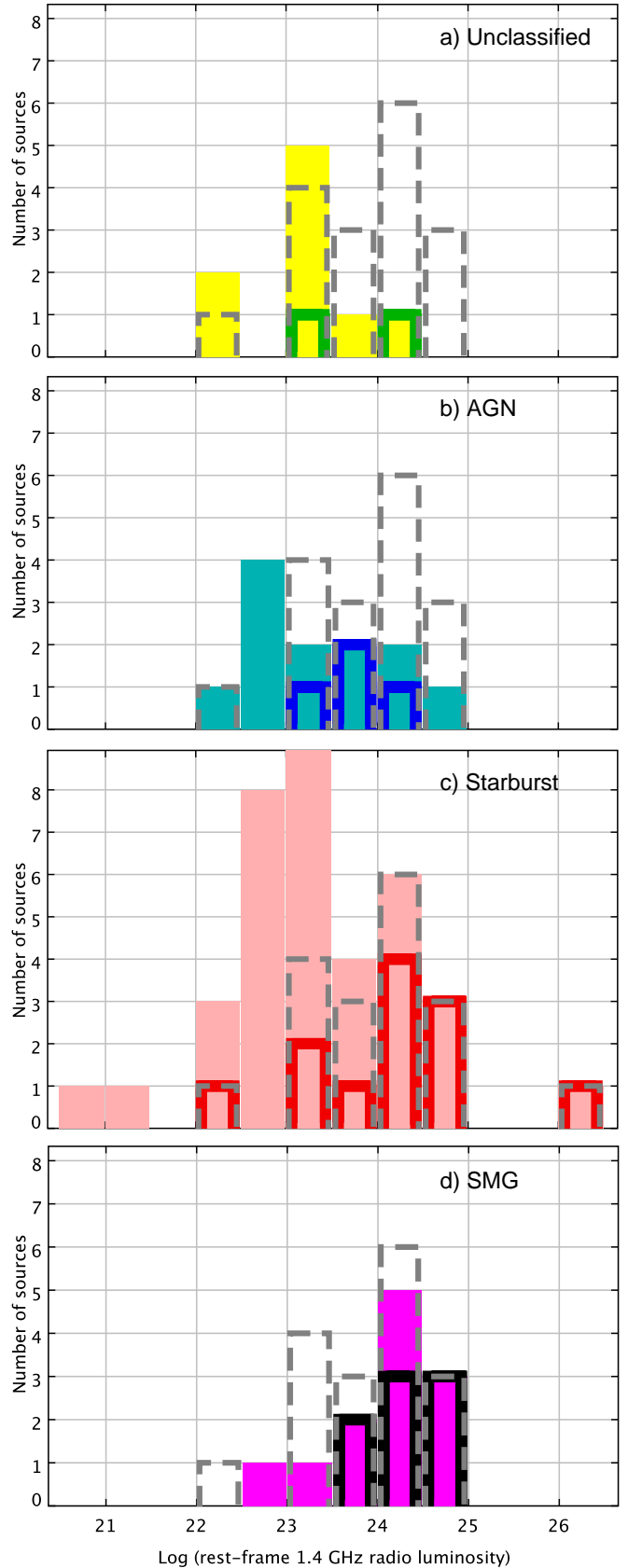


Fig. 9. Radio luminosity distribution of radio/X-ray sources according to radio classification and counterparts, see Fig. 8 for more details.

Table 1. Radio and X-ray sources detected in both regimes. The first 55 were selected at 1.4 GHz (Muxlow et al. 2005). The last 7 were selected at 8.4 GHz (Richards et al. 1998). Columns (1)–(8) give the name, position, flux density (at the selection frequency), spectral index and uncertainties of radio sources. Columns (9)–(11) give the redshift, its uncertainty and the reference (see footnote). Column (12) gives the separation between the radio and X-ray peaks. Columns (13)–(17) give the number, position, flux density, photon index and uncertainties of X-ray sources (Alexander et al. 2003b). Numbers in *italics* signify values of α or Γ estimated from single measurements, and photometric redshifts. Column (18) indicates whether the object was detected by *ISO* (I), *Spitzer* (S) or SCUBA (SMM). See text for further details of crossmatching and estimating uncertainties not given in the original papers.

Name	RA	Dec	$S_{\text{R1.4}}$	LAS	α	$\sigma_{\alpha-}$	$\sigma_{\alpha+}$	z	σ_z	Ref.	Sep.	ABB	F_x	Γ	$\sigma_{\Gamma-}$	$\sigma_{\Gamma+}$	IR/SMM
(1)	(J2000) (2)	(J2000) (3)	(μJy) (4)	($''$) (5)	(6)	(7)	(8)	(9)	(10)	(11)	($''$) (12)	(13)	($10^{-18} \text{ W m}^{-2}$) (14)	(15)	(16)	(17)	(18)
J123606+620951	12 36 06.6128	+62 09 51.141	196	0.9	>0.56	0.07	1.14	0.6379	0.003	CBHCS04	0.31	76	3.22	<−0.91	0.16	0.09	–
J123606+621021	12 36 06.8493	+62 10 21.437	74	0.7	0.80	0.50	0.90	2.51	0.003	CSWMI04	0.08	79	0.74	<0.12	0.37	0.6	SMM
J123608+621035	12 36 08.1195	+62 10 35.898	217	0.6	0.36	0.08	0.08	0.681	0.003	CBHCS04	0.10	82	1.89	0.18	0.21	0.20	–
J123608+621553	12 36 08.2421	+62 15 53.094	59	0.5	−0.24	0.10	0.90	0.4593	0.003	CBHCS04	0.15	83	3.57	−0.32	0.18	0.18	S
J123612+621138	12 36 12.0272	+62 11 38.733	75	1.2	0.80	0.50	0.90	0.275	0.003	CBHCS04	0.14	93	17.71	1.41	0.04	0.04	–
J123616+621513	12 36 16.1419	+62 15 13.937	53	1.0	0.80	0.50	0.90	2.58	0.003	CSWMI04	0.33	109	1.02	0.97	0.21	0.19	SMM
J123617+621011	12 36 17.0801	+62 10 11.306	62	0.6	0.40	0.50	1.30	0.845	0.003	H+01	0.33	113	4.95	1.55	0.08	0.08	–
J123618+621635	12 36 18.0170	+62 16 35.270	47	2.5	0.00	0.50	1.40	0.679	0.003	H+01	0.29	115	15.64	1.45	0.04	0.04	–
J123619+621252	12 36 19.4784	+62 12 52.581	108	0.4	>0.80	0.09	0.90	0.473	0.003	CBHCS04	0.27	119	0.24	1.4	0.6	0.6	–
J123621+621109	12 36 21.2256	+62 11 09.007	52	3.2	>0.86	0.17	0.84	1.014	0.003	C+00	0.23	127	3.86	−0.73	0.21	0.21	–
J123622+621544	12 36 22.4753	+62 15 44.776	83	3.1	>0.60	0.11	0.80	0.6471	0.003	CBHCS04	0.57	132	0.32	1.06	0.48	0.38	S
J123622+621629	12 36 22.6535	+62 16 29.718	70	1.3	0.80	0.50	0.90	2.4	0.003	CSWMI04	0.09	135	1.02	<−0.5	0.25	0.5	SMM
J123624+621743	12 36 24.7685	+62 17 43.160	78	0.9	0.40	0.80	1.30	–	–	–	0.55	143	0.47	<0.29	0.46	0.6	–
J123629+621046	12 36 29.1240	+62 10 45.984	81	2.7	>0.86	0.11	0.84	1.013	0.003	C+00	0.13	158	2.31	0.18	0.16	0.15	S,SMM
J123630+620923	12 36 30.0516	+62 09 23.895	46	0.6	0.80	0.50	0.90	0.953	0.003	B+02	0.20	164	1.93	<−0.77	0.19	0.23	–
J123631+620957	12 36 31.2450	+62 09 57.791	152	0.8	>0.99	0.07	0.71	–	–	–	0.49	167	0.21	1.4	0.6	0.6	–
J123632+620759	12 36 32.5583	+62 07 59.846	90	2.6	>0.58	0.11	1.12	1.9939	0.003	CBHCS04	0.23	171	1.83	0.05	0.23	0.22	SMM
J123633+621005	12 36 33.7269	+62 10 05.962	46	1.2	>0.98	0.19	0.72	1.016	0.003	CBHCS04	0.48	177	0.86	1.42	0.22	0.19	S
J123634+621213	12 36 34.4701	+62 12 13.006	233	1.2	0.74	0.06	0.06	0.456	0.003	CBHCS04	0.07	180	0.44	1.96	0.32	0.28	I,S
J123634+621241	12 36 34.5168	+62 12 41.107	230	1.0	0.74	0.06	0.06	1.219	0.003	C+00	0.15	182	0.29	>1.63	0.37	0.28	I,S,SMM
J123635+621424	12 36 35.5839	+62 14 24.049	87	0.3	>0.87	0.10	0.83	2.011	0.003	D+01	0.06	190	2.52	0.25	0.14	0.13	I,S,SMM
J123636+621320	12 36 36.9061	+62 13 20.337	50	0.7	0.80	0.50	0.90	–	–	–	0.34	196	0.41	0.1	0.48	0.47	–
J123641+620948	12 36 41.5511	+62 09 48.232	75	0.6	>0.56	0.12	1.14	0.518	0.003	C+00	0.15	217	1.48	−0.65	0.38	0.43	S
J123642+621331	12 36 42.0916	+62 13 31.426	467	0.4	0.94	0.06	0.06	4.424	0.003	W+99	0.22	220	0.28	1.35	0.40	0.34	I
J123642+621545	12 36 42.2123	+62 15 45.521	150	1.7	0.50	0.07	0.07	0.857	0.003	H+01	0.09	222	2.46	1.22	0.14	0.13	I
J123644+621133	12 36 44.3870	+62 11 33.145	1290	12.0	0.30	0.05	0.05	1.05	0.003	C+00	0.18	230	0.24	1.4	0.6	0.6	I
J123645+620754	12 36 45.8620	+62 07 54.190	48	3.0	0.40	0.80	1.30	1.433	0.003	CBHCS04	0.47	237	0.34	>1.1	0.9	0.37	–
J123646+621448	12 36 46.0629	+62 14 48.713	124	0.5	0.84	0.12	0.86	–	–	–	0.19	239	0.08	1.4	0.6	0.6	–
J123646+621404	12 36 46.3321	+62 14 04.693	179	0.5	−0.04	0.06	0.06	0.961	0.003	CBHCS04	0.02	240	24.63	0.67	0.04	0.04	I,S
J123646+621445	12 36 46.7360	+62 14 45.640	117	2.3	0.98	0.15	0.15	–	–	–	0.28	243	0.09	1.4	0.6	0.6	–

Table 1. continued.

Name	RA	Dec	$S_{\text{R1.4}}$	LAS	α	$\sigma_{\alpha-}$	$\sigma_{\alpha+}$	z	σ_z	Ref.	Sep.	ABB	F_x	Γ	$\sigma_{\Gamma-}$	$\sigma_{\Gamma+}$	IR/SMM
(1)	(J2000)	(J2000)	(μJy)	($''$)	(6)	(7)	(8)	(9)	(10)	(11)	($''$)	(13)	($10^{-18} \text{ W m}^{-2}$)	(15)	(16)	(17)	(18)
J123646+620833	12 36 46.6587	+62 08 33.291	80	0.8	>0.61	0.11	1.09	0.9712	0.003	CBHCS04	0.59	244	0.17	1.4	0.6	0.6	–
J123649+621313	12 36 49.7432	+62 13 13.065	49	1.0	0.72	0.15	0.15	0.475	0.003	C+00	0.27	260	0.16	1.4	0.6	0.6	I,S,SMM
J123651+621030	12 36 51.1223	+62 10 30.955	95	1.2	0.74	0.17	0.17	0.41	0.003	C+00	0.59	265	0.21	>1.61	0.39	0.31	I,S
J123651+621221	12 36 51.7258	+62 12 21.435	49	1.2	0.71	0.12	0.12	2.71	0.2	CBDP03	0.06	267	2.94	0.56	0.12	0.12	I,S
J123652+621444	12 36 52.8839	+62 14 44.076	168	1.3	−0.12	0.07	0.07	0.321	0.003	CBHCS04	0.05	274	0.46	2.1	0.33	0.29	–
J123653+621139	12 36 53.3629	+62 11 39.647	65	0.3	0.77	0.12	0.12	1.275	0.003	C+00	0.07	277	0.21	>1.93	0.07	0.26	I
J123655+620808	12 36 55.9397	+62 08 08.163	106	0.7	>0.85	0.09	0.85	0.792	0.003	CBHCS04	0.66	288	0.25	>1.35	0.65	0.32	S
J123656+621301	12 36 56.9170	+62 13 01.783	49	1.2	>1.22	0.16	0.48	0.474	0.003	C+00	0.18	294	0.76	1.8	0.23	0.21	I
J123659+621449	12 36 59.9150	+62 14 49.503	47	1.0	0.80	0.50	0.90	0.761	0.003	CBHCS04	0.30	310	0.11	1.4	0.6	0.6	I
J123701+621146	12 37 01.5745	+62 11 46.814	128	3.0	0.67	0.08	0.08	1.52	0.38	BCB+02	0.69	317	0.09	1.4	0.6	0.6	I,SMM
J123704+620755	12 37 04.1120	+62 07 55.484	50	1.0	0.80	0.50	0.90	1.253	0.003	BCB+02	0.18	331	6.34	1.83	0.08	0.07	–
J123705+621153	12 37 05.8599	+62 11 53.541	52	1.5	>1.27	0.17	0.43	0.902	0.003	CBHCS04	0.25	337	0.12	1.4	0.6	0.6	I
J123707+621408	12 37 07.2209	+62 14 08.208	45	0.9	0.29	0.16	0.16	2.48	0.003	CSWMI04	0.34	347	0.98	0.39	0.25	0.23	SMM
J123708+621056	12 37 08.3663	+62 10 56.049	50	0.7	0.35	0.17	0.17	0.422	0.003	CBHCS04	0.29	353	0.28	>1.46	0.54	0.30	S
J123709+620837	12 37 09.4315	+62 08 37.580	45	0.5	−0.35	0.11	0.11	0.907	0.003	CBHCS04	0.32	358	0.87	1.08	0.31	0.28	–
J123709+620841	12 37 09.7518	+62 08 41.249	72	0.8	0.00	0.40	0.12	0.902	0.003	CBHCS04	0.52	359	0.30	>1.09	0.91	0.43	S
J123711+621330	12 37 11.2549	+62 13 30.846	67	1.2	0.69	0.13	0.13	1.112	0.15	B+02	0.88	366	0.56	0.62	0.31	0.28	–
J123711+621325	12 37 11.9865	+62 13 25.771	132	0.8	>1.16	0.08	0.54	1.99	0.003	CSWMI04	0.38	368	0.92	<−0.44	0.26	0.56	SMM
J123716+621512	12 37 16.3740	+62 15 12.343	187	0.4	0.41	0.09	0.09	0.23	0.003	CBHCS04	0.31	388	0.23	>1.52	0.48	0.32	–
J123716+621643	12 37 16.5410	+62 16 43.799	66	0.9	0.80	0.50	0.90	0.557	0.003	C+00	0.36	389	0.42	0.51	0.47	0.41	–
J123716+621733	12 37 16.6811	+62 17 33.327	346	0.6	>0.76	0.06	0.64	1.146	0.003	CBHCS04	0.22	390	21.69	1.03	0.04	0.04	–
J123716+621007	12 37 16.8252	+62 10 07.401	63	0.7	0.80	0.50	0.90	0.411	0.003	C+00	0.50	392	0.13	1.4	0.6	0.6	–
J123721+621129	12 37 21.2539	+62 11 29.954	382	0.8	−0.28	0.06	0.06	1.56	0.39	C+00	0.30	403	0.51	0.28	0.43	0.40	–
J123725+620856	12 37 25.0112	+62 08 56.374	90	0.4	0.40	0.80	1.30	0.984	0.15	B+02	0.33	416	3.57	0.85	0.13	0.12	–
J123734+620931	12 37 34.2420	+62 09 31.930	142	2.8	0.40	0.80	1.30	0.189	0.003	BCB+02	0.24	436	0.75	>1.17	0.83	0.36	–
Name	RA	Dec	$S_{\text{R8.4}}$	LAS	α	$\sigma_{\alpha-}$	$\sigma_{\alpha+}$	z	σ_z	Ref.	Sep.	ABB	F_x	Γ	$\sigma_{\Gamma-}$	$\sigma_{\Gamma+}$	IR/SMM
(J2000)	(J2000)	(J2000)	(μJy)	($''$)							($''$)		($10^{-18} \text{ W m}^{-2}$)				
J123637+621135	12 36 37.002	+62 11 35.14	17.5	–	0.6	0.2	0.2	0.078	0.003	CBHCS04	1.25	197	0.14	1.4	0.6	0.6	I
J123639+621249	12 36 39.881	+62 12 49.93	9.8	–	1.0	0.3	0.3	0.846	0.003	C+00	0.27	211	0.22	1.3	0.4	0.3	I,S
J123644+621249	12 36 44.017	+62 12 49.98	10.2	–	0.7	0.2	0.2	0.556	0.003	C+96	0.18	227	0.09	1.4	0.6	0.6	I,S
J123648+621427	12 36 48.377	+62 14 27.65	9.8	–	0.7	0.3	0.3	0.139	0.003	CBHCS04	1.24	251	0.22	1.4	0.6	0.6	I,S
J123652+621354	12 36 52.764	+62 13 54.77	7.8	–	<0.4	0.8	0.3	1.355	0.003	CBHCS04	0.69	272	0.13	1.4	0.6	0.6	SMM
J123655+621311	12 36 55.402	+62 13 11.41	12.3	–	<0.3	0.7	0.3	0.955	0.003	CBHCS04	0.39	286	1.23	1.5	0.1	0.1	–
J123658+621434	12 36 58.720	+62 14 34.61	11.4	–	<0.4	0.8	0.3	0.678	0.003	CBHCS04	0.96	304	9.18	1.6	0.05	0.05	–

Table 1. continued: References

B+02	Bauer et al. (2002b)
BCB+02	Barger et al. (2002)
C+96	Cohen et al. (1996)
C+00	Cohen (2001)
CBDP03	Conselice et al. (2003)
CBHCS04	Cowie et al. (2004b)
CSWMI04	Chapman et al. (2004b)
D+01	Dawson et al. (2001)
H+01	Hornschemeier et al. (2001)
W+99	Waddington et al. (1999)

Table 2. Luminosity and classification of cross-matched radio and X-ray sources. Columns (1) and (2) give the radio name and rest-frame 1.4-GHz luminosity, columns (3) and (4) give the lower and upper luminosity bounds and column (5) gives the radio-based classification where SB = starburst, AGN = AGN and U = unclassified. Columns (6) and (7) give the source number from Alexander et al. (2003) and the 0.5-8 keV X-ray luminosity, columns (8) and (9) give the lower and upper luminosity bounds and column (10) indicates whether the hard-band X-ray luminosity is $> 10^{35}$ W, indicating an X-ray AGN (AGN-X), or is also classified as an X-ray selected type-II AGN (AGN-II) listed by Padovani et al. (2005). The first 55 sources were selected at 1.4 GHz and the last 7 at 8.4 GHz, references as in Table 1.

Name	L_R W Hz ⁻¹	L_{Rmin} W Hz ⁻¹	L_{Rmax} W Hz ⁻¹	Class (radio)	ABB	L_X W	L_{Xmin} W	L_{Xmax} W	X-ray AGN?
(1)	(2)	(3)	(4)	(5)	(6)	(7)	(8)	(9)	(10)
J123606+620951	2.45E23	2.27E23	3.83E23	U	76	1.19E35	1.05E35	1.35E35	AGN-II
J123606+621021	4.04E24	1.45E24	8.64E24	SB	79	4.91E35	1.07E35	7.42E35	AGN-II
J123608+621035	2.84E23	2.63E23	3.05E23	AGN	82	1.34E35	1.14E35	1.55E35	AGN-II
J123608+621553	2.58E22	2.21E22	3.53E22	SB	83	1.04E35	9.33E34	1.14E35	AGN-II
J123612+621138	1.53E22	1.24E22	1.94E22	SB	93	3.29E35	3.19E35	3.40E35	AGN-X
J123616+621513	3.14E24	1.08E24	6.79E24	SB	109	2.10E36	1.54E36	2.71E36	AGN-II
J123617+621011	1.36E23	9.09E22	2.46E23	U	113	1.19E36	1.11E36	1.26E36	AGN-X
J123618+621635	5.08E22	3.50E22	8.87E22	AGN	115	2.13E36	2.07E36	2.20E36	AGN-X
J123619+621252	7.50E22	6.81E22	1.01E23	SB	119	1.42E34	9.79E33	1.91E34	no
J123621+621109	2.41E23	1.94E23	3.88E23	SB	127	2.92E35	2.44E35	3.41E35	AGN-II
J123622+621544	1.09E23	9.73E22	1.54E23	SB	132	3.22E34	2.32E34	4.29E34	no
J123622+621629	3.35E24	1.26E24	7.06E24	SB	135	2.92E35	1.07E35	3.96E35	AGN-II
J123624+621743	–	–	–	U	143	–	–	–	AGN-II
J123629+621046	3.75E23	3.28E23	5.99E23	SB	158	3.30E35	2.87E35	3.76E35	AGN-II
J123630+620923	1.74E23	1.08E23	2.84E23	SB	164	1.31E35	1.05E35	1.55E35	AGN-II
J123631+620957	–	–	–	U	167	–	–	–	no
J123632+620759	1.97E24	1.66E24	4.41E24	U	171	7.50E35	5.52E35	9.59E35	AGN-II
J123633+621005	2.33E23	1.82E23	3.58E23	SB	177	2.95E35	2.46E35	3.48E35	AGN-X
J123634+621213	1.45E23	1.36E23	1.54E23	SB	180	2.98E34	2.50E34	3.52E34	no
J123634+621241	1.57E24	1.46E24	1.69E24	SB	182	1.82E35	1.32E35	2.45E35	AGN-X
J123635+621424	2.69E24	2.29E24	5.16E24	SB+AGN	190	1.30E36	1.09E36	1.53E36	AGN-II
J123636+621320	–	–	–	SB	196	–	–	–	no
J123641+620948	5.82E22	5.13E22	8.67E22	SB	217	4.57E34	3.54E34	5.56E34	AGN-X
J123642+621331	1.87E26	1.65E26	2.08E26	SB+AGN	220	4.13E36	1.65E36	7.05E36	AGN-II?
J123642+621545	3.62E23	3.33E23	3.91E23	SB+AGN	222	4.99E35	4.46E35	5.56E35	AGN-X
J123644+621133	4.39E24	4.13E24	4.65E24	AGN	230	8.78E34	4.59E34	1.30E35	no
J123645+620754	3.73E23	1.00E23	8.10E23	U	237	2.02E35	1.19E35	3.74E35	AGN-X
J123646+621448	–	–	–	U	239	–	–	–	no
J123646+621404	3.94E23	3.65E23	4.23E23	AGN	240	4.46E36	4.31E36	4.62E36	AGN-II
J123646+621445	–	–	–	U	243	–	–	–	no

Table 2. continued.

Name	L_R W Hz ⁻¹	L_{Rmin} W Hz ⁻¹	L_{Rmax} W Hz ⁻¹	Class (radio)	ABB	L_X W	L_{Xmin} W	L_{Xmax} W	X-ray AGN?
(1)	(2)	(3)	(4)	(5)	(6)	(7)	(8)	(9)	(10)
J123646+620833	2.80E23	2.45E23	4.90E23	SB	244	5.17E34	2.45E34	8.03E34	AGN-X
J123649+621313	3.33E22	2.81E22	3.84E22	SB	260	9.61E33	6.49E33	1.30E34	no
J123651+621030	4.65E22	4.13E22	5.17E22	SB	265	9.84E33	7.54E33	1.25E34	no
J123651+621221	2.96E24	2.06E24	3.86E24	SB	267	3.94E36	3.04E36	4.86E36	AGN-II
J123652+621444	3.74E22	3.48E22	4.01E22	AGN	274	1.44E34	1.24E34	1.66E34	no
J123653+621139	5.14E23	4.33E23	5.96E23	SB	277	1.89E35	1.37E35	2.29E35	AGN-X
J123655+620808	2.60E23	2.34E23	3.91E23	U	288	4.59E34	3.04E34	6.84E34	no
J123656+621301	4.02E22	3.39E22	4.97E22	SB	294	5.30E34	4.64E34	6.03E34	no
J123659+621449	1.01E23	6.91E22	1.55E23	SB	310	1.89E34	1.01E34	2.88E34	no
J123701+621146	1.48E24	4.83E23	2.48E24	SB	317	8.12E34	7.01E33	1.58E35	AGN-X
J123704+620755	3.87E23	2.18E23	6.77E23	SB	331	5.03E36	4.70E36	5.40E36	AGN-X
J123705+621153	2.32E23	1.88E23	3.06E23	SB	337	3.06E34	1.56E34	4.69E34	no
J123707+621408	1.25E24	9.39E23	1.57E24	SB	347	8.91E35	6.14E35	1.19E36	AGN-II
J123708+621056	2.28E22	1.88E22	2.67E22	SB	353	1.32E34	1.03E34	1.71E34	no
J123709+620837	7.18E22	5.80E22	8.55E22	AGN	358	1.83E35	1.40E35	2.31E35	AGN-X
J123709+620841	1.42E23	1.02E23	1.61E23	AGN	359	6.28E34	3.87E34	1.05E35	AGN-X
J123711+621331	3.49E23	2.17E23	4.80E23	AGN	366	1.31E35	8.22E34	1.82E35	AGN-II
J123711+621325	5.44E24	4.79E24	8.68E24	SB	368	2.19E35	8.06E34	2.93E35	AGN-II
J123716+621512	2.38E22	2.21E22	2.56E22	AGN	388	3.00E33	2.32E33	3.80E33	no
J123716+621643	6.72E22	5.02E22	9.52E22	SB	389	2.41E34	1.72E34	3.20E34	no
J123716+621733	2.05E24	1.90E24	3.06E24	AGN	390	7.37E36	7.10E36	7.64E36	AGN-II
J123716+621007	3.16E22	2.48E22	4.23E22	SB	392	5.69E33	3.00E33	8.73E33	no
J123721+621129	1.94E24	9.10E23	2.97E24	AGN	403	1.71E35	6.39E34	2.83E35	AGN-X
J123725+620856	2.82E23	9.50E22	5.54E23	U	416	7.68E35	5.10E35	1.02E36	AGN-X
J123734+620931	1.20E22	1.00E22	1.49E22	U	436	6.10E33	4.41E33	8.13E33	no
J123637+621135	7.17E20	1.62E20	1.62E20	SB	197	1.92E32	5.75E31	5.75E31	no
J123639+621249	1.87E23	7.34E22	7.34E22	SB	211	4.55E34	1.24E34	1.44E34	no
J123644+621249	3.47E22	2.40E22	4.53E22	SB	227	7.65E33	4.40E33	1.08E34	no
J123648+621427	1.60E21	5.48E20	5.48E20	SB	251	9.87E32	2.13E32	2.13E32	no
J123652+621354	1.08E23	8.44E22	4.89E22	U	272	8.81E34	5.13E34	5.13E34	AGN-X
J123655+621311	5.75E22	2.85E22	1.48E22	AGN	286	3.84E35	4.03E34	4.03E34	AGN-X
J123658+621434	3.09E22	1.61E22	1.08E22	U	304	1.35E36	5.02E34	5.02E34	AGN-X

